# A novel IRE1 kinase inhibitor for adjuvant glioblastoma treatment

Diana Pelizzari Raymundo, Dimitrios Doultsinos, Raphaël Pineau, Chloé Sauzay, Thodoris Koutsandreas, Timothy Langlais, Antonio Carlesso, Elena Gkotsi, Luc Negroni, Tony Avril, et al.

iScience

CellPress
OPEN ACCESS

Article

# A novel IRE1 kinase inhibitor for adjuvant glioblastoma treatment

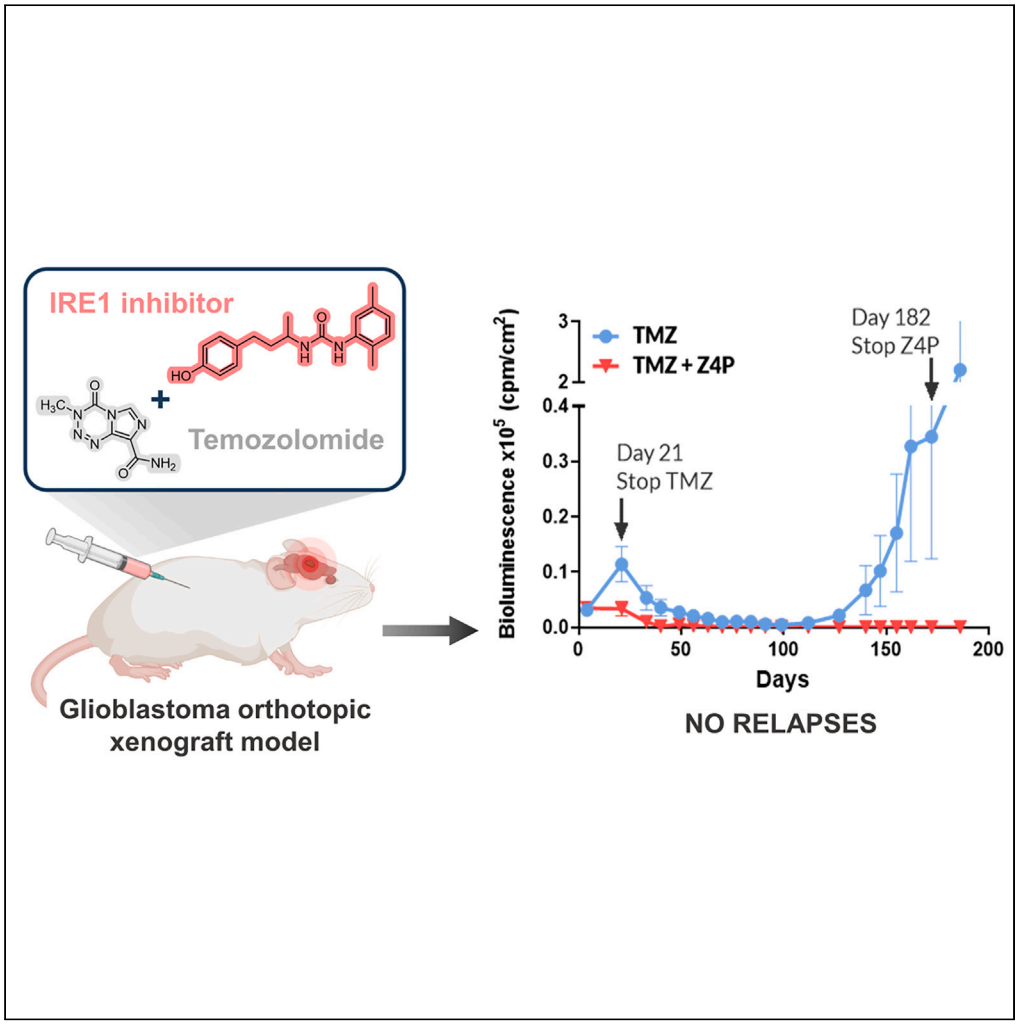


Diana Pelizzari-Raymundo, Dimitrios Doultsinos, Raphael Pineau, ..., Eric Chevet, Leif A. Eriksson, Xavier Guillory

eric.chevet@inserm.fr (E.C.)
leif.eriksson@chem.gu.se (L.A.E.)
xavier.guillory@univ-rennes1.fr (X.G.)

## Highlights

*In silico* screening yields a structurally new and brain-permeable IRE1 inhibitor

Co-treatment with temozolomide prevents glioblastoma relapses in mice

Validation of IRE1 as a therapeutic target for adjuvant treatment in glioblastoma

Pelizzari-Raymundo et al., iScience *26*, 106687
May 19, 2023 
https://doi.org/10.1016/j.isci.2023.106687

iScience

CellPress
OPEN ACCESS

Article

# A novel IRE1 kinase inhibitor for adjuvant glioblastoma treatment

Diana Pelizzari-Raymundo,[1,2,8] Dimitrios Doultsinos,[1,2,8] Raphael Pineau,[1,2] Chloé Sauzay,[1,2] Thodoris Koutsandreas,[4,5] Timothy Langlais,[3] Antonio Carlesso,[6] Elena Gkotsi,[4,5] Luc Negroni,[7] Tony Avril,[1,2] Aristotelis Chatziioannou,[4,5] Eric Chevet,[1,2,9,10,*] Leif A. Eriksson,[6,9,*] and Xavier Guillory[1,2,3,9,*]

## SUMMARY

**Inositol-requiring enzyme 1 (IRE1) is a major mediator of the unfolded protein response (UPR), which is activated upon endoplasmic reticulum (ER) stress. Tumor cells experience ER stress due to adverse microenvironmental cues, a stress overcome by relying on IRE1 signaling as an adaptive mechanism. Herein, we report the discovery of structurally new IRE1 inhibitors identified through the structural exploration of its kinase domain. Characterization in *in vitro* and in cellular models showed that they inhibit IRE1 signaling and sensitize glioblastoma (GB) cells to the standard chemotherapeutic, temozolomide (TMZ). Finally, we demonstrate that one of these inhibitors, Z4P, permeates the blood–brain barrier (BBB), inhibits GB growth, and prevents relapse *in vivo* when administered together with TMZ. The hit compound disclosed herein satisfies an unmet need for targeted, non-toxic IRE1 inhibitors and our results support the attractiveness of IRE1 as an adjuvant therapeutic target in GB.**

## INTRODUCTION

The unfolded protein response (UPR), mediated by PKR-like ER kinase (PERK), activating transcription factor 6 (ATF6), and inositol-requiring enzyme 1 alpha (IRE1α, referred to as IRE1 hereafter), plays instrumental roles in disease development by transducing signals from the endoplasmic reticulum (ER) lumen to the nucleus. These three transducers of the UPR have been identified as potential therapeutic targets in cancer as well as other diseases.[1] In particular, the modulation of IRE1 activity as therapeutic intervention in multiple diseases has been the subject of extensive preclinical investigations.[2,3] IRE1 signaling depends on both its kinase and ribonuclease domains to produce functional outputs. The ATP-binding kinase domain enables IRE1 phosphorylation necessary to activate the RNase domain which has two distinct functional outputs. Firstly, it unconventionally splices *XBP1* mRNA to produce XBP1s, a potent transcription factor, and secondly, it cleaves a subset of mRNAs and miRNAs in a process called regulated IRE1-dependent decay (of RNA) – RIDD to ease transcriptional load. Small-molecule IRE1 modulators may target the ATP-binding kinase pocket, the RNase domain,[4] or allosteric sites.[5] Kinase-inhibiting RNase attenuators (KIRAs) that bind the kinase pocket have a direct inhibitory effect on IRE1 RNase activity[6,7] while other IRE1 kinase inhibitors indirectly inhibit the RNase by impeding IRE1 phosphorylation.[8] Conversely, all IRE1 inhibitors that directly bind the RNase domain share a common hydroxy aryl aldehyde core that allows the formation of a reversible covalent imine bond with IRE1 Lysine 907. This class of compounds encompasses early inhibitors such as 4μ8c,[9,10] STF-083010,[11] and the later developed MKC compounds,[12] including MKC8866 (recently renamed ORIN1001), which is under clinical trial (NCT03950570) for advanced solid tumors as single agent or for relapsed refractory breast cancer in combination with Abraxane.[13]

The properties of IRE1 as a pro-survival signaling mediator are particularly evident in cancer, as tumor cells utilize a hyper-adaptive UPR to overcome physiological, metabolic, or therapeutic stresses. This makes IRE1 inhibition an attractive therapeutic option in oncology, evidenced by preclinical studies targeting multiple myeloma,[12,14,15] prostate cancer,[16] acute myeloid leukemia,[17,18] and triple-negative breast cancer (TNBC).[19,20] Collectively, these studies demonstrate that IRE1 inhibition may be used as monotherapy or as adjuvant therapy alongside standard of care against various cancers including glioblastoma (GB), the most common primary tumor of the CNS according to the World Health Organization. GB is an aggressive,

[1]INSERM U1242, Université de Rennes, Rennes, France

[2]Centre de Lutte contre le Cancer Eugène Marquis, Rennes, France

[3]Univ Rennes, CNRS, ISCR – UMR 6226, 35000 Rennes, France

[4]e-NIOS PC, Kallithea-Athens, Greece

[5]Center of Systems Biology, Biomedical Research Foundation of the Academy of Athens, Athens, Greece

[6]Department of Chemistry and Molecular Biology, University of Gothenburg, Göteborg, Sweden

[7]Proteomics platform, Institut de Génétique et de Biologie Moléculaire et Cellulaire (IGBMC)/INSERM U964/CNRS UMR 7104/Université de Strasbourg, Illkirch, France

[8]These authors contributed equally

[9]These authors contributed equally

[10]Lead contact

*Correspondence: eric.chevet@inserm.fr (E.C.), leif.eriksson@chem.gu.se (L.A.E.), xavier.guillory@univ-rennes1.fr (X.G.)

https://doi.org/10.1016/j.isci.2023.106687

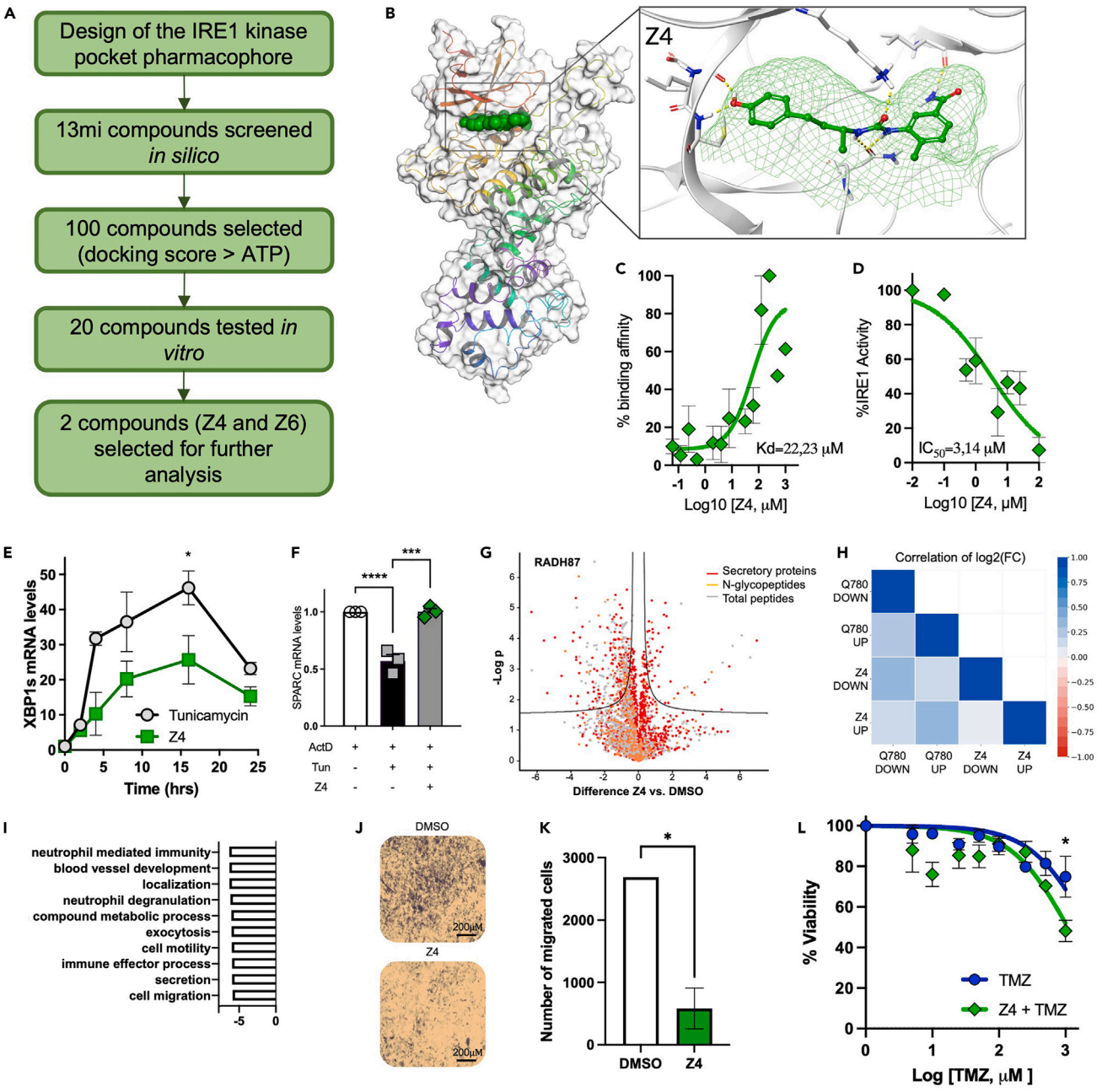


**Figure 1. Pipeline of Z4 discovery and its characterization *in vitro* and in cells**

(A) The screening based on pharmacophore modeling led to the identification of Z4 as a putative IRE1 inhibitor candidate.

(B) Glide docking pose of Z4 in IRE1 ATP-binding pocket (PDB: 3P23).

(C) Human recombinant IRE1 (n = 3) protein was used as fluorescently labeled target at final concentrations of 20 nM in microscale thermophoresis experiments. Z4 was used as ligand in the indicated concentration range. The experimental data were normalized, and fitted to a saturation one-site binding equation. Kd values calculated from the fit are shown in the figure.

(D) Activity of IRE1 in the presence of increasing concentrations of Z4 from FRET signal given out upon fluorescent probe cleavage over 25 min incubation. The IC50 derived from the fitting curves are indicated in the figure. Symbols and error bars represent mean values ±SEM.

(E) Quantification of XBP1s mRNA levels upon treatment with 1 µg/mL tunicamycin over 24 h in the presence or absence of pre-treatments with 25 µM Z4 normalized to untreated U87 cells.

(F) Quantification of SPARC mRNA levels in the presence of 5 µg/ml Actinomycin D and presence or absence of 10 µg/mL tunicamycin and 25 µM Z4 over 4 h in U87 cells.

**Figure 1. *Continued***

(G–I) Functional comparison of GB cell line RADH87 proteome upon treatment with Z4 or in lines genetically impaired for IRE1 signaling (expressing an IRE1 Q780stop variant).

(J) Migration assay of RADH87 cell line on Boyden Chambers in the presence or not of Z4 treatment over 24 h.

(K) Quantification of the experiments presented in J, the average ± SEM of 3 independent experiments.

(L) Cell viability of U87 cells as function of TMZ concentration, in the presence of increasing concentrations of Z4. The non-linear regression was calculated using the GraphPad Prism software. Symbols and error bars represent mean values ±SEM. *p values ≤0.05, ***p values ≤0.001, ****p values ≤0.0001, E, F,: ANOVA, K: *t*-test.

highly recurrent, and highly heterogeneous cancer. Most patients succumb to the disease despite a comprehensive therapeutic standard-of-care (SOC) protocol comprising maximal safe surgical resection followed by a combination of irradiation and chemotherapy with the alkylating agent temozolomide (TMZ; STUPP protocol).[21] To cope with a hostile microenvironment, GB cells need to maintain high metabolic rates and consequently cope with heightened protein synthesis/folding demands[22] through activation of UPR signaling.[23] Indeed, genetic ablation of IRE1 activity in GB preclinical models was shown to give rise to smaller and less aggressive tumors[24,25] while an IRE1 activity signature correlated high IRE1/XBP1s activity with worse prognoses in GB patient cohorts.[26] To test the effectiveness of IRE1 RNase pharmacological inhibition against GB development and recurrence, we established a preclinical murine GB surgical model that fully recapitulates human SOC.[27] This model was used to implement a hydrogel loaded with the non-brain-penetrant MKC8866 for *in situ* release in mouse brains. We showed that SOC and MKC8866 co-administration had modest beneficial effects on mouse survival compared to SOC alone, due to the limited bioavailability of MKC8866 (*i.e.* single dose, local application).

We have shown that IRE1 inhibition is an attractive therapeutic option in GB; however, none of the compounds currently reported in the literature present adequate physicochemical properties for use in CNS diseases. As such, there is an urgent need for identifying an IRE1 inhibitor that can passively cross the blood–brain barrier (BBB) to treat GB. In this study, we identify and characterize a structurally original, BBB-permeable IRE1 inhibitor that has a profound effect on IRE1 activity *in vitro* and in cell-based models. When administered together with TMZ *in vivo*, it sensitizes GB models to TMZ, preventing tumor relapse with minimal side effects, enhancing the efficacy of established GB treatments.

## RESULTS

We have previously described a drug discovery pipeline which uses structural analysis of the IRE1 crystal structure, leading to the identification of FDA-approved compounds that can inhibit IRE1 activity *in vitro* and sensitize cellular models of GB to TMZ.[28] Despite providing clinically relevant information on drug repurposing and pharmacovigilance, we found that these drugs i) did not meet our criteria for optimal GB targeting as they could not cross the BBB, ii) have known clinical toxicity profiles, and iii) are not specific binders to IRE1 itself. To address these issues, we used our drug discovery pipeline on a much larger chemical library to identify small molecules fulfilling a specific set of criteria: to i) be able to specifically bind to IRE1's cytosolic domain; ii) display low toxicity in experimental GB models *in vitro* and *in vivo*; (iii) to block IRE1 activity *in vitro* and *in vivo*; iv) cross the BBB; v) sensitize GB experimental models to chemotherapy *in vitro* and *in vivo*; and vi) have no previously described clinical designation.

Identification of structurally new IRE1 modulator candidates through an *in silico* pharmacophore screen - Applying the IRE1 modulator discovery pipeline,[28] we screened the ZINC15[29] database to identify compounds able to bind onto the ATP-binding pocket of the IRE1 kinase domain. For that, we utilized pharmacophore binding hypotheses between the IRE1 kinase domain and fragments of the IRE1 structure itself[26,28] (Figure 1A). The resulting compound library was then computationally docked onto the IRE1 ATP-binding pocket using Glide Dock of the Schrödinger Maestro Suite. To limit chances of unspecific and weak binding, we set a threshold for the docking score of each compound corresponding to the docking score of the kinase pocket natural substrate, ATP (Table S2). Only compounds with docking scores superior to ATP were considered for further investigation. The two best candidates, named Z4 and Z6, were chosen to be further characterized and tested to validate their ability to modulate IRE1 activity *in vitro*. Z6 presented a high toxicity profile (not shown) and consequently was excluded from further analysis. Z4 displayed a much more favorable toxicity profile and was extensively tested for its ability to modulate IRE1 activity (Figure 1A).

### IRE1-fragment-derived organic molecules dock onto the ATP-binding pocket of IRE1 *in silico* and *in vitro*

Z4 is a small (MW 341.40 g/mol), urea-based compound bearing a *para*-substituted phenol. Z4 is predicted to interact with the ATP-binding pocket through van der Waals interactions and hydrogen bonding with the phenolic hydroxyl group to hinge residue Cys645 and with the urea's heteroatoms in the central part of the molecules with Asp711 and Asp688 or Lys690, located in the phosphate-binding region of the pocket (Figure 1B). All dockings were performed using Glide extra precision (XP) mode[30] and the OPLS-2005 force field.[31]

Interestingly, of the different compounds obtained, none (including Z4 and Z6) was identified as a key binder using the sulfonamide-"KIRA-like"-bound crystal structure (PDB: 4U6R), in which ligand binding induces a shift outward of the αC-helix, rupture of the Lys-Glu bridge, and dealignment of the R-spine. This slight distortion relative to the ATP-bound form has been claimed to be the key factor of the ability of the KIRA compounds to attenuate RNase activity.[32] The compounds were instead obtained as top hits from screening against the ATP-bound structure (PDB: 3P23), yet, as seen below, are nonetheless highly efficient in blocking RNase activity. This may be indicative that the compounds described in this work have a mechanism of action different from the KIRA compounds that remain to be characterized. To quantify the binding affinity between IRE1 and the compound, we performed microscale thermophoresis (MST) using increasing concentrations of Z4 in the presence of recombinant IRE1 protein. We show that IRE1 interacts with Z4 following a saturation one-site binding curve exhibiting respective $K_D$ of ~20 μM (Figure 1C). Z4 was next tested for inhibitory activity using a fluorescence-quenched IRE1 RNA substrate probe. This yielded $IC_{50}$s in the low micromolar range (Figure 1D and Table S3).

### Z4 attenuates IRE1 RNase activity *in vitro* and in cellular models of GB

Having demonstrated that Z4 docks to IRE1 *in silico*, binds to IRE1, and inhibits its RNase activity in clean *in vitro* systems, we proceeded to investigate whether this compound could affect IRE1 activity in *in vitro* GB cellular models. Since kinase interference may mediate RNase effects[33] and since IRE1 has two distinct functional outputs through its RNase domain (XBP1 splicing and RIDD), we investigated the effect of Z4 on *XBP1* mRNA splicing and RIDD-mediated RNA degradation. We found that Z4 inhibits tunicamycin-induced *XBP1* mRNA splicing in U87 cells (Figure 1E). We next tested Z4 effects on RIDD by measuring mRNA levels of known RIDD target SPARC[34] in U87 cells treated with actinomycin D and tunicamycin. Z4 blocked tunicamycin-induced degradation of *SPARC* mRNA compared to control treatment (Figure 1F) while it had no effect in cells overexpressing a dominant-negative form of IRE1 (Figure S1A).

We next investigated whether Z4 impacted other arms of the UPR. This was to ensure that the related stress responses were specific to Z4 action on IRE1 rather than other UPR transducers. To this end, we evaluated the expression of downstream effectors of PERK and ATF6 signaling. Neither *CHOP* nor *HERPUD1* mRNA expression was significantly affected upon treatment with Z4 (Figures S1B–S1C). Moreover, eIF2α phosphorylation and ATF4 protein expression were not altered upon Z4 treatment (Figure S1D). These experiments indicated that Z4 did not significantly impact other branches of the UPR than the IRE1 arm.

To document the effects of Z4 treatment at the protein level, we monitored its impact on the proteome of RADH87 (a human tumor-derived primary GB cell line[35]) cells. Treatment of RADH87 cells with Z4 impacted on pathways such as immunity, circulatory system development, cell locomotion, and cell migration; all properties involved in tumor establishment (*e.g.* angiogenesis) and tumor invasion (*e.g.* metastasis) (Figures 1G–1I and S2). We then compared the proteomes of Z4-treated cell lines to the same cell line overexpressing a truncated mutant form of IRE1 lacking an RNase domain known to blunt IRE1 activity[26] (Figures 1H and S2). Remarkably, proteome alterations upon Z4 exposure phenocopied those observed in cells in which IRE1 activity was genetically blunted (Figure 1H), thus reinforcing the selectivity of Z4 toward IRE1 signaling (Figures 1G–1I). Cell migration emerged as a key mechanism affected by Z4 treatment. To confirm this, migratory capacity of 3 different GB cell lines (U251, RADH85, and RADH87) was tested in the presence or absence of Z4. We found that Z4 treatment systematically reduced cell migration (Figures 1J, 1K, and S3). Interestingly, the primary lines RADH85 and RADH87 were the most impacted by Z4 (Figures 1J, 1K, and S3). Having extensively documented the effect and specificity of this inhibitor on IRE1 activity, we hypothesized that it may sensitize GB cells to TMZ in a similar fashion as reported in TNBC with paclitaxel.[20] Cell viability assays were carried out on U87 cells treated with sub-toxic doses of Z4 and escalating doses of TMZ. Cell viability at the point of maximal TMZ administration decreased by

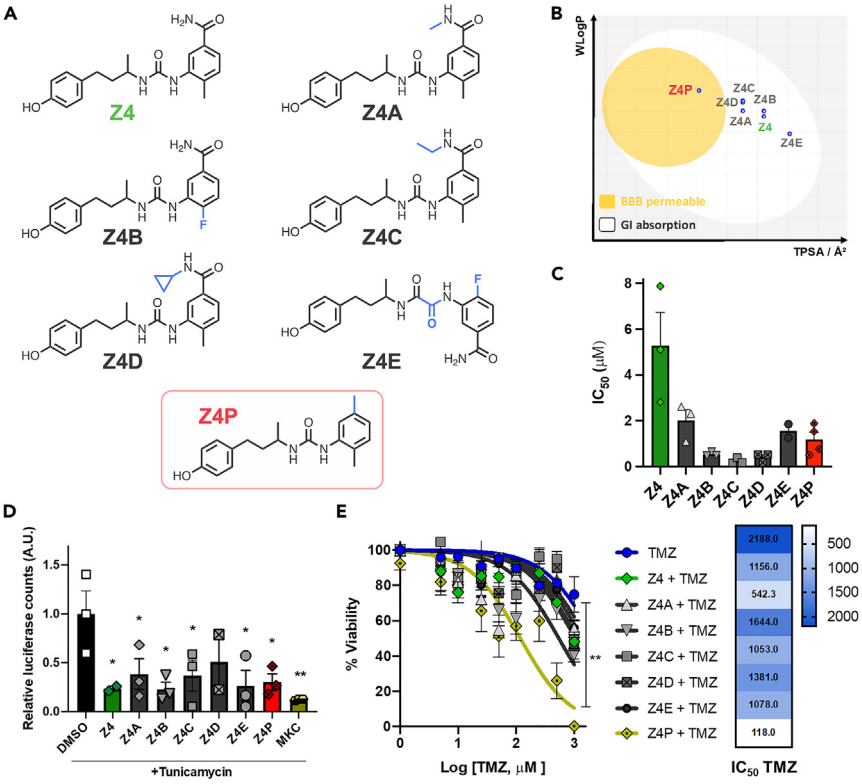


**Figure 2. Z4-derived compounds inhibit IRE1 activity in cellular models**

(A) The bidimensional organic structures of Z4A-Z4E and Z4P.

(B) The top compounds described in (A) were further assessed for their capability to cross the blood–brain barrier, using the egg yolk graphical representation from SwissADME where the lipophilicity, represented by LogP (calculated according to the method developed by Wildman and Crippen (WLOGP)), is plotted against the topological polar surface area (TPSA). Compound Z4P was selected for further investigation on top of Z4A-E based on its predicted ability to cross the BBB.

(C) The $IC_{50}$ of Z4-derived compounds calculated from fluorescence signals obtained from fluorescent probe cleavage over 25 min incubation.

(D) Relative luciferase counts of HEK cells transfected with XBP1-reporter and treated or not with Z4 analogs and MKC8866 for 1 h prior to ER stress induction using 2.5 µg/mL tunicamycin.

(E) Cell viability of U87 cells in the presence of increasing concentrations of TMZ. The non-linear regression was calculated using the GraphPad Prism software. $IC_{50}$ of TMZ for each condition was calculated using the equation model Y = 100/(1 + 10^(X-LogIC50)). Symbols and error bars represent mean values ±SEM. *p values ≤0.05, **p values ≤0.01, C,D: ANOVA, E: *t*-test.

1.5-fold in the presence of Z4 compared to control (Figure 1L), an effect recapitulated in primary RADH87 cells (Figure S4).

Collectively, these results show that Z4 fulfills most criteria set out at the beginning of this investigation for a potential IRE1 therapeutic. However, ADME properties predictions for this molecule showed a sub-optimal profile for BBB passive permeation, and as such, Z4 could not prove its validity *in vivo*.

## Identification of a BBB-permeable Z4 derivative

We next tried to identify BBB-permeable Z4 derivatives. Z4 was used as a template to identify a group of structurally similar small molecules by applying a Tanimoto similarity coefficient.[36] After docking the top 100 similar-to-Z4 hits to the IRE1 crystal structure, we selected the top compounds with docking scores superior to that of Z4 and predicted their BBB-crossing capabilities by two *in silico* approaches (QikProp from the Maestro Suite and the online tool swissADME[37]). This process identified a single compound (Z4P) that was predicted to cross the BBB (Figures 2A and 2B and Table 1). To further validate our drug

**Table 1. Z4 family members and key physicochemical properties for passive BBB permeation compared to the median values of marketed CNS drugs**

| ADME Property | cLogP | Hydrogen Bond Donors | Topological Polar Surface Area (Å$^2$) | Rotatable bonds |
|---|---|---|---|---|
| Attributes of a Successful CNS Drug | 2–4 | ≤3 | <90 | <8 |
| Z4 QikProp | 1.767 | 5 | 120.48 | 7 |
| Z4 swissADME | 2.57 | 4 | 104.45 | 8 |
| Z4A QikProp | 2.89 | 4 | 105.25 | 7 |
| Z4A swissADME | 2.91 | 4 | 90.46 | 9 |
| Z4B QikProp | 1.79 | 5 | 120.48 | 7 |
| Z4B swissADME | 2.5 | 4 | 104.45 | 8 |
| Z4C QikProp | 3.32 | 4 | 104.37 | 8 |
| Z4C swissADME | 3.23 | 4 | 90.46 | 10 |
| Z4D QikProp | 3.54 | 4 | 104.14 | 8 |
| Z4D swissADME | 3.30 | 4 | 90.46 | 10 |
| Z4E QikProp | 4.05 | 3 | 66.59 | 6 |
| Z4E swissADME | 2.1 | 4 | 121.52 | 9 |
| Z4P QikProp | 3.80 | 3 | 66.54 | 6 |
| Z4P swissADME | 3.67 | 3 | 61.36 | 7 |

Compounds possessing properties in range with known successful CNS drugs have a high probability of passively crossing the BBB (does not take into account active transporter proteins).[38] Data were predicted using the open web-server SwissADME and Schrodinger's built-in tool QikProp (Maestro version 2018-1).

discovery pipeline, we retained five additional candidates with the best docking scores (Z4A-E) (Figure 2A and Table 2) to compare the effects of those compounds on IRE1 signaling *in vitro* and as a retrospective cross-validation control to show that our *in silico* pipeline could robustly identify IRE1 modulators (Figures 2A and 2B). We next characterized the Z4 derivatives as we did with their precursor Z4. The $IC_{50}$ of these molecules was determined *in vitro* by a fluorescence-quenched IRE1 RNA substrate probe (Figure S5) and the values are shown on Figure 2C. As predicted from the docking scores values determined *in vitro*, all the top 6 analogs (Z4A-E and Z4P) exhibited lower $IC_{50}$ than Z4.

We evaluated Z4's and Z4P's ability to cross the BBB in a human *in vitro* model.[39] Predictably, only Z4P was demonstrated to passively permeate the BBB. More specifically, Z4 can be classified as low-permeable compound according to its permeability ($p = 3.1 \pm 10^{-6}$ cm/s). The asymmetry in the transport being higher from basal to apical (BA/AB ratio = 18.8). This ratio is comparable to the control molecule prazosin that was included in the study as a breast cancer resistance protein (BCRP) substrate, suggesting that Z4 could be a substrate of efflux transporters such as p-glycoprotein, BCRP, and multidrug resistance protein. Such efflux transporters are likely to be involved if BA ratio > AB ratio, meaning that the drug is actively transported out of the brain. On the other hand, Z4P is a highly permeable compound ($p = 20.4 \pm 10^{-6}$ cm/s), with a good permeability in both directions (BA/AB ratio = 1.1), comparable to the positive control verapamil (BA/AB ration = 1.0), a lipophilic drug known to easily cross the BBB. The integrity of the cell layers was assessed by measuring the *trans*-endothelial electrical resistance (TEER) and by monitoring Lucifer Yellow (LY) permeation. The high TEER and low paracellular permeability of LY (Table S4) shows that the barrier stability of the model was maintained during the incubation with the compounds, confirming the absence of significant toxic effect.

To confirm IRE1 inhibition data obtained *in vitro*, we next performed a luciferase-based assay on HEK cells transfected with XBP1-luc reporter[40] treated with Z4 and its derivatives under tunicamycin-induced ER

**Table 2. Z4 family members molecular weights and docking scores (docking scores were obtained using Glide XP (extra precision) docking utilizing Maestro version 2018-1)**

| | Z4 | Z4A | Z4B | Z4C | Z4D | Z4E | Z4P |
|---|---|---|---|---|---|---|---|
| Molecular Weight (Da) | 341.40 | 355.43 | 345.37 | 369.46 | 381.47 | 373.38 | 312.41 |
| Docking score | −7.406 | −9.060 | −8.984 | −8.524 | −8.239 | −8.040 | −7.394 |

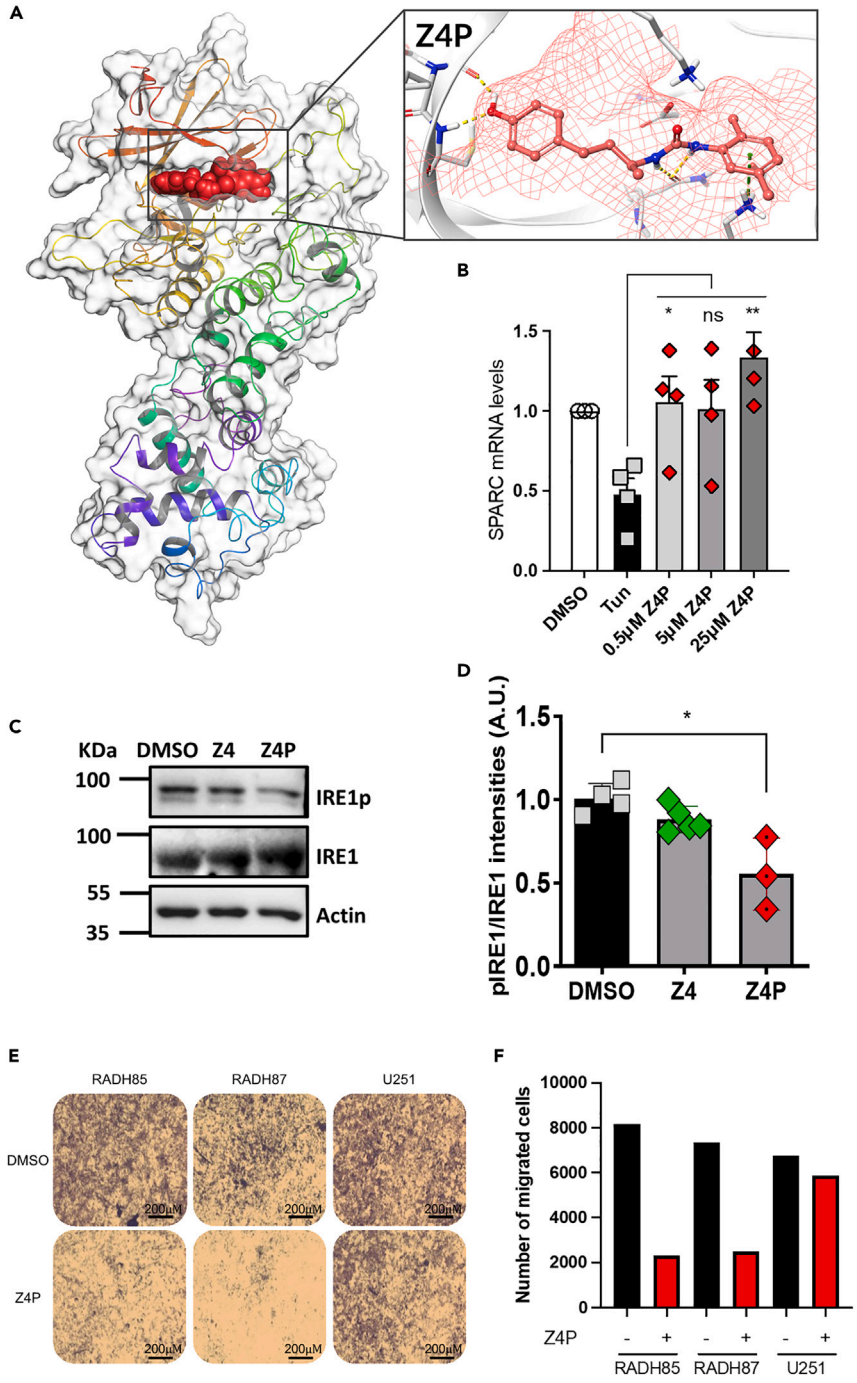


**Figure 3. Z4P interacts with the ATP-binding pocket of IRE1 *in silico* and *in vitro* and inhibits IRE1 activity in cellular models**

(A) Glide docking poses of Z4P in IRE1 ATP-binding pocket (PDB: 3P23).

(B) Quantification of SPARC mRNA levels in the presence of 5 μg/ml actinomycin D and presence or absence of 10 μg/mL tunicamycin and increasing concentrations of Z4P over 4 h in U87 cells.

(C) Protein levels of IRE1 and phospho-IRE1 in U87 cells treated with Z4 and Z4P over 24 h.

(D) Fold change of protein expression between IRE1 and phospho-IRE1 is represented in bar chart form normalized to untreated U87 cells.

(E) Migration assay of U251 and the primary lines RADH85 and RADH87 on Boyden Chambers in the presence or not of Z4P treatment over 24 h.

**Figure 3. *Continued***
(F) Quantification of the experiments presented in E. Different GB cell lines (RADH85, RADH87, and U251) were treated (red bars) or not (black bars) with Z4P. Symbols and error bars represent mean values ±SEM. ns: non-significant, *p values ≤0.05, **p values ≤0.01, B, D: ANOVA, F: *t*-test.

stress. Figure 2D shows that *XBP1* mRNA splicing was impaired when the cells were treated with Z4-family compounds. MKC8866 was used as a control of IRE1 inhibition. To test if inhibition of IRE1 by Z4 derivatives sensitizes GB cells to TMZ, we performed cell viability assays with TMZ alone or in combination with Z4-family compounds, showing all molecules to sensitize cells to TMZ (Figure 2E). Surprisingly, Z4P drastically decreased the $IC_{50}$ of TMZ in comparison with the other Z4-family compounds, reinforcing its potential as a chemotherapy adjuvant (Figure 2E). *In silico* experiments suggested that Z4P is able to interact with IRE1 with a similar binding mode to its prototype Z4 within the same IRE1 pocket (Figure 3A).

Z4P, like Z4, can inhibit XBP1 splicing. However, Z4P possesses a stereocenter. As such, we tested if both enantiomers would have the same effect on IRE1 inhibition by synthesizing the racemic compound and separating the enantiomers by chiral chromatography. Both enantiomers, named Z4P (*S*) and Z4P (*R*), were used in the IRE1-mediated *in vitro* cleavage assay and the luciferase XBP1-luc reporter assay in HEK293T cells as described above. Figures S6 and S7 show that both enantiomers inhibit IRE1 activity. Based on their $IC_{50}$ values (Figures S6 and S7) as well as MST data (not shown), we determined that both enantiomers are able to bind to IRE1 in a competitive manner.

As seen for the XBP1 pathway, Z4P was also able to inhibit the other pathway of IRE1 (RIDD) in U87 cells upon treatment with actinomycin D and tunicamycin, avoiding the tunicamycin-induced degradation of *SPARC* mRNA[34] compared to control (Figure 3B). Upstream of these effects, we also monitored the phosphorylation state of IRE1 under Z4P treatments in U87 cells. Figures 3C, 3D and S8 show that IRE1 phosphorylation is reduced under Z4 compounds treatments. In order to guarantee that the treatments with these compounds would not produce any major off-target effects, kinase profiling was performed to determine the selectivity of both Z4 and Z4P. As shown by their respective kinome phylogenetic trees (Figure S9) at a concentration of 10 μM, both compounds demonstrated to have very little effect on other kinases with no more than 20% inhibition across the panel (Table S5). Finally, we evaluated the effects of Z4P on migration of RADH85, RADH87 (primary cell lines), and U251 (ATCC HTB-17) cells (Figures 3E and 3F). Z4P was able to attenuate migration, in all the cell lines tested, with higher efficacy in the primary cell lines (RADH85; RADH87).

Overall, Z4P was extensively characterized *in vitro* and was proven to be effective in our GB cell models, thus emerging as a legitimate candidate for *in vivo* validation from our pool of Z4-derived compounds.

## Combination therapy of Z4P and TMZ against *in vivo* models of GB arrests tumor growth and prolongs relapse-free survival

To characterize Z4P *in vivo*, we utilized murine models growing orthotopic tumors generated by intracranial injection of U87-luc cells (25). First, we administered intra-peritoneal (IP) escalating doses of Z4P (60 μg/kg to 300 μg/kg) to determine Z4P systemic toxicity *in vivo*. The maximum dose was determined based on stability and solubility features of the compound. Above this concentration, the solubility was affected and therefore no concentration above 300 μg/kg was used. No toxicity was detected in wild-type (WT) mice in any of the concentrations tested (Figure S10A). Since Z4P displayed zero toxicity in WT mice, we then sought to i) characterize the effect of Z4P on IRE1 biology in an *in vivo* tumor; ii) test the capacity of Z4P to cross the BBB and reach tumor cells in our model; and iii) determine if co-treatment of Z4P alongside SOC chemotherapy TMZ conferred any anti-tumorigenic, anti-relapse, or pro-survival advantages. To this end, U87-luc cells were orthotopically implanted in the mouse brain and the tumor was allowed to grow. At day 4 post implantation, a small tumor formation was detected using bioluminescence (*data not shown*). Thereafter, mice were randomized in different groups and Z4P daily treatments (i.p. 300 μg/kg) were administered for 30 consecutive days (Figure 4A). Upon completion of this time period, mouse brains were entirely excised and dissected. The corresponding tumors were resected, dissociated, and RNA was extracted from them. The splicing of *XBP1* mRNA was evaluated in control tumors and in Z4P-treated animals. Treatment with Z4P decreased the splicing of *XBP1* mRNA thus demonstrating that Z4P mediates IRE1 inhibition in *in vivo* tumors when administered IP, further validating its ability to cross the BBB *in vivo* (Figure 4B). Brain samples from each group, control and Z4P, were resected and

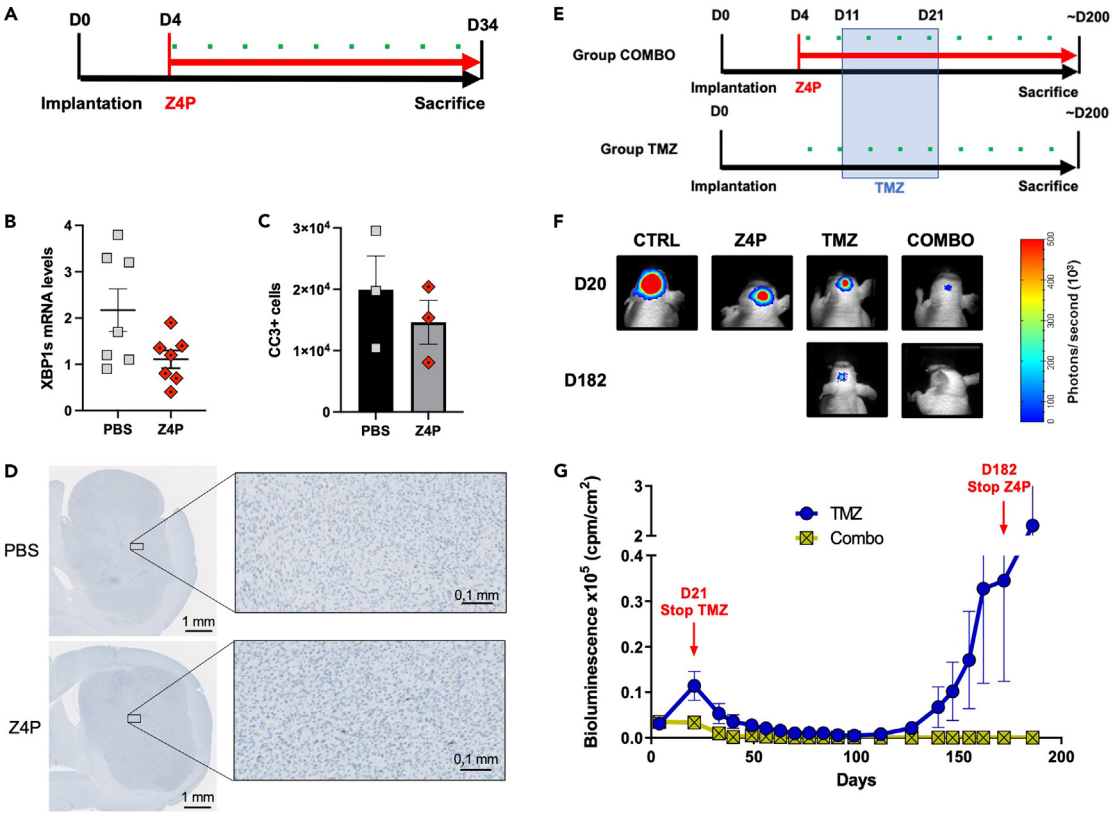


**Figure 4. Z4P crosses the BBB, delays relapse *in vivo* under TMZ treatment**

(A) Treatment timeline for Z4P at 300 μg/kg/day (red) in GB model over 34 days. Period of tumor monitoring is expressed in green.

(B) Quantification of XBP1s mRNA levels from *in vivo* tumors upon treatment with Z4P against the control.

(C and D) Immunohistochemistry of Cleavage Caspase 3 (CC3+) in brains from mice treated or not with Z4P.

(E) Treatment timeline for combination of Z4P (red) and TMZ (blue) in GB model over 186 days. Period of tumor monitoring is expressed in green.

(F) Tumor growth monitored by bioluminescence imaging. The bioluminescence images of the tumor-bearing mice from the groups treated with TMZ alone or in combination with Z4P (COMBO) at days 20 and 182 post-U87 cells implantation.

(G) Time-resolved quantitative analysis of bioluminescence imaging signal over 186 days of experiment for the groups treated with TMZ alone or in combination with Z4P (COMBO). Symbols and error bars represent mean values ±SEM.

immunohistochemistry of cleaved Caspase-3 (Asp175) Antibody (Cell Signaling #9661) was performed. As shown in Figures 4C and 4D, no difference on cleaved Caspase-3 staining between PBS and Z4P was observed which demonstrates that the drug alone is not sufficient to induce cell death by apoptosis.

Finally, we investigated the potential of Z4P as monotherapy or neo-adjuvant therapy alongside TMZ in a clinically relevant, surgical model of GB. Utilizing our Z4P-treated, orthotopic mouse model (i.p. 300 μg/kg daily, starting on D4), we administered 10 daily treatments of TMZ (10 mg/kg; Figure 4E) after day 11 post-tumor cell implantation. While Z4P treatment alone had no effect on tumor growth or mouse survival, co-treatment with TMZ significantly increased survival and decreased tumor growth (Figures 4F and S10B). This effect was observed as early as during the first week of treatment (Figures 4F and 4G). One of the aggressive hallmarks of clinical GB is the very high probability of tumor recurrence despite treatment with TMZ. To this end, we investigated whether co-treatment of Z4P and TMZ would have an effect on tumor recurrence. Over 200 days, expectedly, mice treated with TMZ alone relapsed (Figure 4G, blue curve) forming new tumors; a result consistent with what is observed in the clinic. In contrast, no tumor relapse was observed in the group of animals treated with both TMZ and Z4P (Figure 4G, yellow curve); full panel of samples are presented at D20 and D182 in Figure S11. In conclusion, Z4P, administered intraperitoneally, sensitizes orthotopically implanted GB tumors to TMZ in mice and prevents tumor relapse when used as an adjuvant therapy alongside TMZ. This has major translational clinical implications as GB tumor relapse is the major cause of death in patients and responsible for the dismal prognosis of this cancer.

## DISCUSSION

In the course of cancer evolution, tumor cells must cope with both intrinsic (e.g. aneuploidy, oncogene expression) or extrinsic stresses (e.g. nutrient shortage, therapeutic regimens that may for instance induce DNA damage). IRE1 signaling has been identified as a major adaptive mechanism triggered in cancer cells to cope with these stresses. The rationale behind using IRE1 inhibition against cancer is that by doing so, one may impair tumor growth by blocking adaptive mechanisms triggered by intrinsic stresses, and/or cripple the ability of cancer cells to cope with extrinsic stresses such as those induced by treatments. As such, the pharmacological targeting of IRE1 in cancer represents an appealing therapeutic option. Thus far, the use of pharmacological IRE1 modulators has been tested as mono- or adjuvant therapies alongside conventional or novel treatment regimes. These inhibitors exhibited significant efficacy in attenuating tumor growth and relapse in various preclinical hematological and solid cancer models.[3,11,12,14,16,17,19,20]

In GB, multiple novel therapeutic approaches including immunotherapy or the use of oncolytic viruses have so far presented limited outcomes.[41–44] As such, targeting the tumoral adaptive capacity may lead to improved SOC efficacy through the use of adjuvant treatments. In GB, the IRE1 RNase inhibitor MKC8866 was shown to enhance the efficacy of surgical resection combined with radiation and chemotherapy *in vivo*.[27] However, this molecule does not cross the BBB and required peri-surgical implantation of a drug-containing hydrogel, thereby limiting the drug impact. Moreover, so far, none of the other IRE1 RNase or kinase inhibitors efficiently present adequate physicochemical properties to cross the BBB. Herein, we address this need, by reporting the discovery of a distinct structural class of BBB-permeable IRE1 inhibitors active in mouse brains. More specifically, using our established *in silico* pipeline,[28] we identified a family of molecules (Z4-family) based on a molecular scaffold that differs from known IRE1 modulators. This family of compounds inhibits IRE1 RNase activity *in vitro* and *in vivo*, and does not target the other arms of the UPR. Both genetic- and Z4-mediated IRE1 inhibition impacted the cellular proteome in a similar manner with the modulation of functions related to metabolic and catabolic processes, cell adhesion and locomotion, and essential hallmarks of GB aggressiveness. The global ability of Z4 compounds to sensitize GB cells to TMZ (Figures 2 and S4) together with the ability of the Z4-family member, Z4P, to cross the BBB (Table 1) increased their clinical potential value, thus further justifying investigations in preclinical GB mouse models. *In vivo*, a clear attenuation of *XBP1* mRNA splicing in Z4P-treated tumors suggests the effective penetration of this drug in the brain. We next treated mice with TMZ alone or with a combination of Z4P and TMZ over a period of 200 days to evaluate treatments efficacy and tumor relapse. Z4P monotherapy did not show any impact on tumor growth but mice treated with a combination of Z4P and TMZ showed better first response to chemotherapy and did not relapse in our experimental time frame (Figure 4).

Beyond Z4P, the members of the Z4-family tested herein presented better *in silico* docking scores and *in vitro* $IC_{50}$ than Z4P, thereby indicating that they could also be investigated in other malignancies where BBB crossing is not an issue and to avoid neurological off-target effects. These compounds could for instance be tested alongside docetaxel/paclitaxel in breast cancer,[17,18] bortezomib in advanced multiple myeloma and acute myeloid leukemia,[12,14,15,17] as well as androgen deprivation therapies enzalutamide, abiraterone acetate, and chemotherapy cabazitaxel in prostate cancer models.[16,45] Further investigations are, however, required to map the full repertoire of mechanisms by which Z4P-mediated IRE1 inhibition sensitizes GB cells to chemotherapy. Since IRE1/XBP1s axis is known to play a role on the functioning of immune system,[46] the use of immune-competent mouse models and the addition of radiotherapy in the treatment protocol would be a great advance on the documentation of the mode of action of Z4P. Studies have indicated that blocking *XBP1* mRNA splicing could reduce tumoral pro-survival adaptation against extrinsic stresses while inhibition of RIDD may enhance the effects of DNA-damaging agents.[47] IRE1 is involved in multiple physiological and pathophysiological processes and its activation status varies from patient to patient. Indeed, we have described an IRE1 activity signature that is able to stratify patient cohorts according to their XBP1 or RIDD activation status.[20] Such a tool would be invaluable in determining which patients with GB would best benefit from IRE1 inhibition, thus enhancing the efficacy of molecules such as Z4P alongside SOC. Our work was based on the use of GB cell lines that were characterized as exhibiting a mesenchymal phenotype, the most aggressive type of GB and that also shows the highest basal IRE1 activity.[26] Additional studies should be performed in different models of GB to describe how these compounds could act in different subtypes of GB and in different patients based on their IRE1 signature.[26]

In conclusion, we describe a class of compounds structurally distinct from known modulators able to inhibit IRE1 activity and sensitize GB cells to TMZ-based chemotherapy. A member of this family of compounds,

Z4P, is able to cross the BBB and to blunt IRE1 signaling in an orthotopic mouse model of GB. Indeed, treatment of GB tumors *in vivo* with a combination of both Z4P and TMZ resulted in improved efficacy and prevented tumor relapse. Further studies, currently ongoing in the laboratory, aim to document the molecular mechanisms by which those effects are mediated. In addition, pharmacokinetic and pharmacodynamic assays will be performed in preclinical models. Hence, our results identify Z4P as a promising hit compound for adjuvant treatment in GB that needs to be further improved on several parameters such as stability, bioavailability, potency, affinity, and proteolytic stability, a hit-to-lead process currently ongoing in our laboratory.

### Limitations of the study

This work described a novel *in silico* drug discovery pipeline to identify novel IRE1 inhibitors. Among them, we characterized one molecule (Z4P) able to cross the BBB and as such providing a solid foundation to develop, in future, a novel GB treatment in clinics. However, the development and improvement of this novel family of compounds is an urgent matter in order to apply them in the clinic. Indeed, according to our ADMET data, this molecule presents a low solubility and is moderately unstable after 24 h incubation in aqueous solution, which can explain some variability of the *in vitro* results. We have bypassed that in our study in the *in vivo* assays injecting daily doses of Z4P during the experiment. In addition, these novel IRE1 inhibitors were used *in vivo* using a xenogenic orthograft immunodeficient mouse model. Since IRE1/XBP1s signaling is important for the functioning of the immune system, including antibody production, the evaluation of Z4P on immune-competent animals would be of great value. Another limitation of our study is that the combination of Z4P and TMZ used inhibited the relapse over a very long time frame (~200 days), after which the animals had to be sacrificed due to other diseases not related with the tumor. This precluded us from determining any long-term effect of the treatment. Lastly, to better understand the effect of this combination and to mimic what is done in the clinics, experiments in mice using resection followed by radiotherapy and chemotherapy should be performed.

## STAR★METHODS

Detailed methods are provided in the online version of this paper and include the following:

- KEY RESOURCES TABLE
- RESOURCE AVAILABILITY
  - Lead contact
  - Materials availability
  - Data and code availability
- EXPERIMENTAL MODEL AND SUBJECT DETAILS
  - Animal model
- METHOD DETAILS
  - Materials
  - Chemical syntheses
  - Racemic Z4P synthesis
  - *In silico* drug analyses
  - MicroScale Thermophoresis (MST)
  - IRE1-mediated *in vitro* RNase assay
  - Cell treatments
  - Quantitative real-time PCR
  - Luciferase assays
  - Western blotting
  - Migration assay
  - Kinome selectivity profiling
  - Tumor cell orthotopic implantation
  - Mouse treatments
  - Bioluminescence monitoring
  - Immunohistochemistry
  - Quantification and statistical analysis

## SUPPLEMENTAL INFORMATION

Supplemental information can be found online at https://doi.org/10.1016/j.isci.2023.106687.

## ACKNOWLEDGMENTS

We thank Dr Frédéric Delom, Dr Delphine Fessart, Pr Reynald Gillet, Dr David Gillot, Dr Élodie Lafont, Dr Eric Ogier-Denis, and Pr Afshin Samali for the critical reading of the manuscript. Part of this work was carried out using the Spectroscopies-CDTP core facility, the animal facility ARCHE, and the immunohistochemistry platform H2P2 (UMS Biosit, Université de Rennes 1- Campus de Villejean - 35043 RENNES Cedex, FRANCE). This work was supported by grants from Institut National du Cancer (INCa; PLBIO), Agence Nationale de la Recherche (ANR; ERAAT), Fondation pour la Recherche Médicale (FRM; DEQ20180339169), the EU COST action 861952 "Proteocure" and Cancéropôle Grand-Ouest (Gliotreat) to E.C.; EU H2020 MSCA ITN-675448 (TRAINERS) and MSCA RISE-734749 (INSPIRED) grants to E.C., A.C., and L.A.E.; INSERM (International Research Project – TUPRIC) to A.C. and E.C.; La Ligue contre le Cancer (comités 22, 35, 36, 56 et 85), INSERM, Région Bretagne and from the institut des Neurosciences Cliniques de Rennes (INCR) to T.A. The Swedish Research Council (VR; grant no 2019-3684)), the Swedish Cancer Foundation (grant no 21-1447 Pj) and the Swedish National Infrastructure for Computing (SNIC; funded in part through VR grant agreement 2018-05973) are gratefully acknowledged for funding and allocations of computing time, respectively (L.A.E.). D.P.R. was funded by grants from INSERM (LA VANNETAISE) and the Brittany Region, D.D. was funded by EU H2020 MSCA ITN-675448, C.S. was funded by a Plan Cancer post-doctoral fellowship, X.G. was funded by the Fondation ARC pour la recherche sur le cancer, grant PDF20191209830, C.S. was funded by a post-doctoral fellowship from INSERM-plan cancer.

## AUTHOR CONTRIBUTIONS

D.P.R., D.D., X.G. - conceptualization, methodology, investigation, writing. A.Ca., R.P., T.L., T.K., C.S., L.N., E.G. – methodology, investigation; A.C., E.C., L.A.E., T.A., X.G. – supervision, conceptualization, project administration, funding acquisition; writing (https://www.casrai.org/credit.html#).

## DECLARATION OF INTERESTS

L.A.E. and E.C. are founders of Cell Stress Discoveries Ltd. A.C. is a founder of e-NIOS Applications PC (https://e-nios.com/). L.A.E. is founder of ANYO Labs (www.anyoloabs.com). E.C. is founder of Thabor therapeutics (https://www.thabor-tx.com/). A patent (PCT/EP2023/050228) cover the discovery in this work.

## INCLUSION AND DIVERSITY

We support inclusive, diverse, and equitable conduct of research.

Received: December 1, 2022
Revised: February 27, 2023
Accepted: April 13, 2023
Published: April 24, 2023

## REFERENCES

1. Grandjean, J.M.D., and Wiseman, R.L. (2020). Small molecule strategies to harness the unfolded protein response: where do we go from here? J. Biol. Chem. *295*, 15692–15711. https://doi.org/10.1074/jbc.REV120.010218.

2. Hetz, C., Axten, J.M., and Patterson, J.B. (2019). Publisher Correction: pharmacological targeting of the unfolded protein response for disease intervention. Nat. Chem. Biol. *15*, 1129. https://doi.org/10.1038/s41589-019-0363-x.

3. Raymundo, D.P., Doultsinos, D., Guillory, X., Carlesso, A., Eriksson, L.A., and Chevet, E. (2020). Pharmacological targeting of IRE1 in cancer. Trends Cancer *6*, 1018–1030. https://doi.org/10.1016/j.trecan.2020.07.006.

4. Langlais, T., Pelizzari-Raymundo, D., Mahdizadeh, S.J., Gouault, N., Carreaux, F., Chevet, E., Eriksson, L.A., and Guillory, X. (2021). Structural and molecular bases to IRE1 activity modulation. Biochem. J. *478*, 2953–2975. https://doi.org/10.1042/BCJ20200919.

5. Amarasinghe, K.N., Pelizzari-Raymundo, D., Carlesso, A., Chevet, E., Eriksson, L.A., and Jalil Mahdizadeh, S. (2022). Sensor dimer disruption as a new mode of action to block the IRE1-mediated unfolded protein response. Comput. Struct. Biotechnol. J. *20*, 1584–1592. https://doi.org/10.1016/j.csbj.2022.03.029.

6. Wang, L., Perera, B.G.K., Hari, S.B., Bhhatarai, B., Backes, B.J., Seeliger, M.A., Schürer, S.C., Oakes, S.A., Papa, F.R., and Maly, D.J. (2012). Divergent allosteric control of the IRE1α endoribonuclease using kinase inhibitors. Nat. Chem. Biol. *8*, 982–989. https://doi.org/10.1038/nchembio.1094.

7. Feldman, H.C., Tong, M., Wang, L., Meza-Acevedo, R., Gobillot, T.A., Lebedev, I., Gliedt, M.J., Hari, S.B., Mitra, A.K., Backes, B.J., et al. (2016). Structural and functional analysis of the allosteric inhibition of IRE1α with ATP-competitive ligands. ACS Chem. Biol. *11*, 2195–2205. https://doi.org/10.1021/acschembio.5b00940.

8. Hetz, C., Chevet, E., and Harding, H.P. (2013). Targeting the unfolded protein response in disease. Nat. Rev. Drug Discov. *12*, 703–719. https://doi.org/10.1038/nrd3976.

9. Cross, B.C.S., Bond, P.J., Sadowski, P.G., Jha, B.K., Zak, J., Goodman, J.M., Silverman, R.H., Neubert, T.A., Baxendale, I.R., Ron, D., and Harding, H.P. (2012). The molecular basis for selective inhibition of unconventional mRNA splicing by an IRE1-binding small molecule. Proc. Natl. Acad. Sci. USA *109*, E869–E878. https://doi.org/10.1073/pnas.1115623109.

10. Kemp, K.L., Lin, Z., Zhao, F., Gao, B., Song, J., Zhang, K., and Fang, D. (2013). The serine-threonine kinase inositol-requiring enzyme

1α (IRE1α) promotes IL-4 production in T helper cells. J. Biol. Chem. *288*, 33272–33282. https://doi.org/10.1074/jbc.M113.493171.

11. Ming, J., Ruan, S., Wang, M., Ye, D., Fan, N., Meng, Q., Tian, B., and Huang, T. (2015). A novel chemical, STF-083010, reverses tamoxifen-related drug resistance in breast cancer by inhibiting IRE1/XBP1. Oncotarget *6*, 40692–40703. https://doi.org/10.18632/oncotarget.5827.

12. Mimura, N., Fulciniti, M., Gorgun, G., Tai, Y.-T., Cirstea, D., Santo, L., Hu, Y., Fabre, C., Minami, J., Ohguchi, H., et al. (2012). Blockade of XBP1 splicing by inhibition of IRE1α is a promising therapeutic option in multiple myeloma. Blood *119*, 5772–5781. https://doi.org/10.1182/blood-2011-07-366633.

13. Gabrail, N.Y., Hamilton, E.P., Elias, A.D., Rimawi, M.F., Li, C., Corvez, M.M., Li, W., Feng, Y., Wei, J., Greene, S., et al. (2021). A phase 1/2 trial of ORIN1001, a first-in-class IRE1 inhibitor, in patients with advanced solid tumors. J. Clin. Orthod. *39*, 3080. https://doi.org/10.1200/JCO.2021.39.15_suppl.3080.

14. Ri, M., Tashiro, E., Oikawa, D., Shinjo, S., Tokuda, M., Yokouchi, Y., Narita, T., Masaki, A., Ito, A., Ding, J., et al. (2012). Identification of Toyocamycin, an agent cytotoxic for multiple myeloma cells, as a potent inhibitor of ER stress-induced XBP1 mRNA splicing. Blood Cancer J. *2*, e79. https://doi.org/10.1038/bcj.2012.26.

15. Palumbo, A., Gay, F., Bringhen, S., Falcone, A., Pescosta, N., Callea, V., Caravita, T., Morabito, F., Magarotto, V., Ruggeri, M., et al. (2008). Bortezomib, doxorubicin and dexamethasone in advanced multiple myeloma. Ann. Oncol. *19*, 1160–1165. https://doi.org/10.1093/annonc/mdn018.

16. Sheng, X., Nenseth, H.Z., Qu, S., Kuzu, O.F., Frahnow, T., Simon, L., Greene, S., Zeng, Q., Fazli, L., Rennie, P.S., et al. (2019). IRE1α-XBP1s pathway promotes prostate cancer by activating c-MYC signaling. Nat. Commun. *10*, 323. https://doi.org/10.1038/s41467-018-08152-3.

17. Sun, H., Lin, D.-C., Guo, X., Kharabi Masouleh, B., Gery, S., Cao, Q., Alkan, S., Ikezoe, T., Akiba, C., Paquette, R., et al. (2016). Inhibition of IRE1α-driven pro-survival pathways is a promising therapeutic application in acute myeloid leukemia. Oncotarget *7*, 18736–18749. https://doi.org/10.18632/oncotarget.7702.

18. Kriss, C.L., Pinilla-Ibarz, J.A., Mailloux, A.W., Powers, J.J., Tang, C.-H.A., Kang, C.W., Zanesi, N., Epling-Burnette, P.K., Sotomayor, E.M., Croce, C.M., et al. (2012). Overexpression of TCL1 activates the endoplasmic reticulum stress response: a novel mechanism of leukemic progression in mice. Blood *120*, 1027–1038. https://doi.org/10.1182/blood-2011-11-394346.

19. Harnoss, J.M., Le Thomas, A., Reichelt, M., Guttman, O., Wu, T.D., Marsters, S.A., Shemorry, A., Lawrence, D.A., Kan, D., Segal, E., et al. (2020). IRE1α disruption in triple-negative breast cancer cooperates with antiangiogenic therapy by reversing ER stress adaptation and remodeling the tumor microenvironment. Cancer Res. *80*, 2368–2379. https://doi.org/10.1158/0008-5472.CAN-19-3108.

20. Logue, S.E., McGrath, E.P., Cleary, P., Greene, S., Mnich, K., Almanza, A., Chevet, E., Dwyer, R.M., Oommen, A., Legembre, P., et al. (2018). Inhibition of IRE1 RNase activity modulates the tumor cell secretome and enhances response to chemotherapy. Nat. Commun. *9*, 3267. https://doi.org/10.1038/s41467-018-05763-8.

21. Stupp, R., Mason, W.P., van den Bent, M.J., Weller, M., Fisher, B., Taphoorn, M.J.B., Belanger, K., Brandes, A.A., Marosi, C., Bogdahn, U., et al. (2005). Radiotherapy plus concomitant and adjuvant temozolomide for glioblastoma. N. Engl. J. Med. *352*, 987–996. https://doi.org/10.1056/NEJMoa043330.

22. Doultsinos, D., Avril, T., Lhomond, S., Dejeans, N., Guédat, P., and Chevet, E. (2017). Control of the unfolded protein response in Health and disease. SLAS Discov. *22*, 787–800. https://doi.org/10.1177/2472555217701685.

23. Obacz, J., Avril, T., Le Reste, P.-J., Urra, H., Quillien, V., Hetz, C., and Chevet, E. (2017). Endoplasmic reticulum proteostasis in glioblastoma—from molecular mechanisms to therapeutic perspectives. Sci. Signal. *10*, eaal2323.

24. Drogat, B., Auguste, P., Nguyen, D.T., Bouchecareilh, M., Pineau, R., Nalbantoglu, J., Kaufman, R.J., Chevet, E., Bikfalvi, A., and Moenner, M. (2007). IRE1 signaling is essential for ischemia-induced vascular endothelial growth factor-A expression and contributes to angiogenesis and tumor growth in vivo. Cancer Res. *67*, 6700–6707. https://doi.org/10.1158/0008-5472.CAN-06-3235.

25. Auf, G., Jabouille, A., Guérit, S., Pineau, R., Delugin, M., Bouchecareilh, M., Magnin, N., Favereaux, A., Maitre, M., Gaiser, T., et al. (2010). Inositol-requiring enzyme 1 is a key regulator of angiogenesis and invasion in malignant glioma. Proc. Natl. Acad. Sci. USA *107*, 15553–15558. https://doi.org/10.1073/pnas.0914072107.

26. Lhomond, S., Avril, T., Dejeans, N., Voutetakis, K., Doultsinos, D., McMahon, M., Pineau, R., Obacz, J., Papadodima, O., Jouan, F., et al. (2018). Dual IRE1 RNase functions dictate glioblastoma development. EMBO Mol. Med. *10*, e7929. https://doi.org/10.15252/emmm.201707929.

27. Le Reste, P.J., Pineau, R., Voutetakis, K., Samal, J., Jégou, G., Lhomond, S., Gorman, A.M., Samali, A., Patterson, J.B., Zeng, Q., et al. (2020). Local intracerebral inhibition of IRE1 by MKC8866 sensitizes glioblastoma to irradiation/chemotherapy in vivo. Cancer Lett. *494*, 73–83. https://doi.org/10.1016/j.canlet.2020.08.028.

28. Doultsinos, D., Carlesso, A., Chintha, C., Paton, J.C., Paton, A.W., Samali, A., Chevet, E., and Eriksson, L.A. (2021). Peptidomimetic-based identification of FDA-approved compounds inhibiting IRE1 activity. FEBS J. *288*, 945–960. https://doi.org/10.1111/febs.15372.

29. Sterling, T., and Irwin, J.J. (2015). ZINC 15–ligand discovery for everyone. J. Chem. Inf. Model. *55*, 2324–2337. https://doi.org/10.1021/acs.jcim.5b00559.

30. Friesner, R.A., Murphy, R.B., Repasky, M.P., Frye, L.L., Greenwood, J.R., Halgren, T.A., Sanschagrin, P.C., and Mainz, D.T. (2006). Extra precision Glide: docking and scoring incorporating a model of hydrophobic enclosure for Protein−Ligand complexes. J. Med. Chem. *49*, 6177–6196. https://doi.org/10.1021/jm051256o.

31. Banks, J.L., Beard, H.S., Cao, Y., Cho, A.E., Damm, W., Farid, R., Felts, A.K., Halgren, T.A., Mainz, D.T., Maple, J.R., et al. (2005). Integrated modeling program, applied chemical theory (IMPACT). J. Comput. Chem. *26*, 1752–1780. https://doi.org/10.1002/jcc.20292.

32. Korovesis, D., Rufo, N., Derua, R., Agostinis, P., and Verhelst, S.H.L. (2020). Kinase photoaffinity labeling reveals low selectivity profile of the IRE1 targeting imidazopyrazine-based KIRA6 inhibitor. ACS Chem. Biol. *15*, 3106–3111. https://doi.org/10.1021/acschembio.0c00802.

33. Tirasophon, W., Welihinda, A.A., and Kaufman, R.J. (1998). A stress response pathway from the endoplasmic reticulum to the nucleus requires a novel bifunctional protein kinase/endoribonuclease (Ire1p) in mammalian cells. Genes Dev. *12*, 1812–1824. https://doi.org/10.1101/gad.12.12.1812.

34. Dejeans, N., Pluquet, O., Lhomond, S., Grise, F., Bouchecareilh, M., Juin, A., Meynard-Cadars, M., Bidaud-Meynard, A., Gentil, C., Moreau, V., et al. (2012). Autocrine control of glioma cells adhesion and migration through IRE1alpha-mediated cleavage of SPARC mRNA. J. Cell Sci. *125*, 4278–4287. https://doi.org/10.1242/jcs.099291.

35. Hong, F., Breitling, R., McEntee, C.W., Wittner, B.S., Nemhauser, J.L., and Chory, J. (2006). RankProd: a bioconductor package for detecting differentially expressed genes in meta-analysis. Bioinformatics *22*, 2825–2827. https://doi.org/10.1093/bioinformatics/btl476.

36. Willett, P. (2006). Similarity-based virtual screening using 2D fingerprints. Drug Discov. Today *11*, 1046–1053. https://doi.org/10.1016/j.drudis.2006.10.005.

37. Daina, A., Michielin, O., and Zoete, V. (2017). SwissADME: a free web tool to evaluate pharmacokinetics, drug-likeness and medicinal chemistry friendliness of small molecules. Sci. Rep. *7*, 42717. https://doi.org/10.1038/srep42717.

38. Xiong, B., Wang, Y., Chen, Y., Xing, S., Liao, Q., Chen, Y., Li, Q., Li, W., and Sun, H. (2021). Strategies for structural modification of small molecules to improve blood–brain barrier penetration: a recent perspective. J. Med. Chem. *64*, 13152–13173. https://doi.org/10.1021/acs.jmedchem.1c00910.

39. Di Marco, A., Vignone, D., Gonzalez Paz, O., Fini, I., Battista, M.R., Cellucci, A., Bracacel, E., Auciello, G., Veneziano, M., Khetarpal, V., et al. (2020). Establishment of an in vitro human blood-brain barrier model derived from induced pluripotent stem cells and comparison to a porcine cell-based system. Cells *9*, 994. https://doi.org/10.3390/cells9040994.

40. Yang, Z., Zhang, J., Jiang, D., Khatri, P., Solow-Cordero, D.E., Toesca, D.A.S., Koumenis, C., Denko, N.C., Giaccia, A.J., Le, Q.-T., and Koong, A.C. (2018). A human genome-wide RNAi screen reveals diverse modulators that mediate IRE1α–XBP1 activation. Mol. Cancer Res. *16*, 745–753. https://doi.org/10.1158/1541-7786.MCR-17-0307.

41. Jackson, C.M., Choi, J., and Lim, M. (2019). Mechanisms of immunotherapy resistance: lessons from glioblastoma. Nat. Immunol. *20*, 1100–1109. https://doi.org/10.1038/s41590-019-0433-y.

42. Medikonda, R., Dunn, G., Rahman, M., Fecci, P., and Lim, M. (2021). A review of glioblastoma immunotherapy. J. Neuro Oncol. *151*, 41–53. https://doi.org/10.1007/s11060-020-03448-1.

43. Kim, D.S. (2020). Cancer stem cell plasticity in glioblastoma multiforme: a perspective on future directions in oncolytic virotherapy. Future Oncol. *16*, 2251–2264. https://doi.org/10.2217/fon-2019-0606.

44. Lu, V.M., Shah, A.H., Vallejo, F.A., Eichberg, D.G., Luther, E.M., Shah, S.S., Komotar, R.J., and Ivan, M.E. (2021). Clinical trials using oncolytic viral therapy to treat adult glioblastoma: a progress report. Neurosurg. Focus *50*, E3. https://doi.org/10.3171/2020.11.FOCUS20860.

45. Sheng, X., Arnoldussen, Y.J., Storm, M., Tesikova, M., Nenseth, H.Z., Zhao, S., Fazli, L., Rennie, P., Risberg, B., Wæhre, H., et al. (2015). Divergent androgen regulation of unfolded protein response pathways drives prostate cancer. EMBO Mol. Med. *7*, 788–801. https://doi.org/10.15252/emmm.201404509.

46. Crowley, M.J.P., Bhinder, B., Markowitz, G.J., Martin, M., Verma, A., Sandoval, T.A., Chae, C.-S., Yomtoubian, S., Hu, Y., Chopra, S., et al. (2023). Tumor-intrinsic IRE1α signaling controls protective immunity in lung cancer. Nat. Commun. *14*, 120. https://doi.org/10.1038/s41467-022-35584-9.

47. Dufey, E., Bravo-San Pedro, J.M., Eggers, C., González-Quiroz, M., Urra, H., Sagredo, A.I., Sepulveda, D., Pihán, P., Carreras-Sureda, A., Hazari, Y., et al. (2020). Genotoxic stress triggers the activation of IRE1α-dependent RNA decay to modulate the DNA damage response. Nat. Commun. *11*, 2401. https://doi.org/10.1038/s41467-020-15694-y.

48. Jabouille, A., Delugin, M., Pineau, R., Dubrac, A., Soulet, F., Lhomond, S., Pallares-Lupon, N., Prats, H., Bikfalvi, A., Chevet, E., et al. (2015). Glioblastoma invasion and cooption depend on IRE1α endoribonuclease activity. Oncotarget *6*, 24922–24934. https://doi.org/10.18632/oncotarget.4679.

49. Avril, T., Vauleon, E., Hamlat, A., Saikali, S., Etcheverry, A., Delmas, C., Diabira, S., Mosser, J., and Quillien, V. (2012). Human glioblastoma stem-like cells are more sensitive to allogeneic NK and T cell-mediated killing compared with serum-cultured glioblastoma cells. Brain Pathol. *22*, 159–174. https://doi.org/10.1111/j.1750-3639.2011.00515.x.

50. Samali, A., Fitzgerald, U., Deegan, S., and Gupta, S. (2010). Methods for monitoring endoplasmic reticulum stress and the unfolded protein response. Int J Cell Biol. 830307. https://doi.org/10.1155/2010/830307.

51. Obacz, J., Archambeau, J., Sicari, D., Le Reste, P.J., Pineau, R., Martin, S., Barroso, K., Vlachavas, E., Voutetakis, K., Fainsod-Levi, T., et al. (2020). Novel IRE1-dependent proinflammatory signaling controls tumor infiltration by myeloid cells. Preprint at bioRxiv. https://doi.org/10.1101/533018.

52. Goede, A., Michalsky, E., Schmidt, U., and Preissner, R. (2006). SuperMimic–fitting peptide mimetics into protein structures. BMC Bioinf. *7*, 11. https://doi.org/10.1186/1471-2105-7-11.

53. Pettersen, E.F., Goddard, T.D., Huang, C.C., Couch, G.S., Greenblatt, D.M., Meng, E.C., and Ferrin, T.E. (2004). UCSF Chimera - a visualization system for exploratory research and analysis. J. Comput. Chem. *25*, 1605–1612. https://doi.org/10.1002/jcc.20084.

54. Daina, A., and Zoete, V. (2016). A BOILED-egg to predict gastrointestinal absorption and brain penetration of small molecules. ChemMedChem *11*, 1117–1121. https://doi.org/10.1002/cmdc.201600182.

55. Prischi, F., Nowak, P.R., Carrara, M., and Ali, M.M.U. (2014). Phosphoregulation of Ire1 RNase splicing activity. Nat. Commun. *5*, 3554. https://doi.org/10.1038/ncomms4554.

56. Koutsandreas, T., Binenbaum, I., Pilalis, E., Valavanis, I., Papadodima, O., and Chatziioannou, A. (2016). Analyzing and visualizing genomic complexity for the derivation of the emergent molecular networks. Int. J. Monit. Surveill. Technol. Res. *4*, 30–49. https://doi.org/10.4018/IJMSTR.2016040103.

57. https://bioinfominer.com/(e-NIOS Applications P.C.).

58. Gene Ontology Consortium (2021). The Gene Ontology resource: enriching a GOld mine. Nucleic Acids Res. *49*, D325–D334. https://doi.org/10.1093/nar/gkaa1113.

59. Resnik, P. (1999). Semantic similarity in a taxonomy: an information-based measure and its application to problems of ambiguity in natural language. J. Artif. Intell. Res. *11*, 95–130.

60. Lhomond, S., Pallares, N., Barroso, K., Schmit, K., Dejeans, N., Fazli, H., Taouji, S., Patterson, J.B., and Chevet, E. (2015). Adaptation of the secretory pathway in cancer through IRE1 signaling. Methods Mol. Biol. *1292*, 177–194. https://doi.org/10.1007/978-1-4939-2522-3_13.

## STAR★METHODS

### KEY RESOURCES TABLE

| REAGENT or RESOURCE | SOURCE | IDENTIFIER |
|---|---|---|
| **Antibodies** | | |
| IRE1 (H-109) | Anti-human; rabbit polyclonal; SantaCruz Biotechnologies | sc-20790; RRID: AB_2098712 |
| IRE1 phosphorylated form | pS724-IRE1 antibody (Anti-human; rabbit polyclonal; Abcam | ab48187; RRID: AB_873899 |
| Phosphorylated form of eIF2α | anti-phospho-eIF2α (Ser51) (CellSignalling®) | Antibody #9721; RRID: AB_330951 |
| Actin | β-Actin (C4) SantaCruz Biotechnologies | sc-47778; RRID: AB_626632 |
| VCP | Anti-mouse BD Transduction Lab | 612183; RRID: AB_399554 |
| ATF4 | ATF-4 (D4B8) Rabbit; Abcam | mAb #11815; RRID: AB_2616025 |
| **Biological samples** | | |
| Mouse brains | This paper | |
| **Chemicals, peptides, and recombinant proteins** | | |
| IRE1WT (465–977) with *N*-terminal poly-histidine-tag and GST tag | Sino Biological Europe GmbH, Eschborn, Germany | #11905-H20B |
| mRNA fluorescent probe used for the *in vitro* IRE1 RNase assay (Cy3-CAUGUCCGCAGCG CAUG-BHQ3) | Eurogentec | |
| Tunicamycin | Calbiochem (Merck KGaA, Darmstadt, Germany) | 654380 |
| TRIzol reagent | Fisher Scientific, Invitrogen, Carlsbad, CA, USA | 15596026 |
| Z4 | Enamine | Z940452448 |
| Z4A | Enamine | Z413223742 |
| Z4B | Enamine | Z596214968 |
| Z4C | Enamine | Z433844656 |
| Z4D | Enamine | Z433865760 |
| Z4E | Enamine | Z754120048 |
| Z4P | Enamine | Z409477496 |
| **Critical commercial assays** | | |
| RED-Tris-NTA 2$^{nd}$ Generation | NanoTemper, Munich, Germany | # MO-L018 |
| **Deposited data** | | |
| Proteomics data | This paper | Available through the PRIDE Repository (http://www.ebi.ac.uk/pride) with identifier PXD026908 |
| **Experimental models: Cell lines** | | |
| U87-Luc | Principal Investigator: Michel Moenner Jabouille A., et al.[48] | |
| U87MG | U87; ATCC | HTB-14™ |
| U251MG | Merck | 09063001-1VL |
| RADH85 | Principal Investigator: Véronique Quillien Avril, T., et al. (2012)[49] | |

(*Continued on next page*)

*Continued*

| REAGENT or RESOURCE | SOURCE | IDENTIFIER |
|---|---|---|
| RADH87 | Principal Investigator: Véronique Quillien<br>Avril, T., et al. (2012)[49] | |
| U87 DN | Principal Investigator: Eric Chevet<br>Lhomond, S., et al. (2018)[26] | |
| U87 Q780 | Principal Investigator: Eric Chevet<br>Lhomond, S., et al. (2018)[26] | |
| **Experimental models: Organisms/strains** | | |
| Mouse NMRI-Foxn1nu/Foxn1nu,<br>8 weeks old male mice | Janvier Laboratories, Laval, France | |
| **Oligonucleotides** | | |
| *Xbp1s* | Integrated DNA Technologies | See Table S1 |
| *Actin* | Integrated DNA Technologies | See Table S1 |
| *Sparc* | Integrated DNA Technologies | See Table S1 |
| *Cd133* | Integrated DNA Technologies | See Table S1 |
| *Col6A1* | Integrated DNA Technologies | See Table S1 |
| *Vegfa* | Integrated DNA Technologies | See Table S1 |
| *Olig2* | Integrated DNA Technologies | See Table S1 |
| *Chop* | Integrated DNA Technologies | See Table S1 |
| *Il-6* | Integrated DNA Technologies | See Table S1 |
| *Il-8* | Integrated DNA Technologies | See Table S1 |
| *Sox2* | Integrated DNA Technologies | See Table S1 |
| *Cdh1* | Integrated DNA Technologies | See Table S1 |
| *Herpud1* | Integrated DNA Technologies | See Table S1 |
| *Perk* | Integrated DNA Technologies | See Table S1 |
| *Cd44* | Integrated DNA Technologies | See Table S1 |
| *Sall2* | Integrated DNA Technologies | See Table S1 |
| *Bip* | Integrated DNA Technologies | See Table S1 |
| *Atf4* | Integrated DNA Technologies | See Table S1 |
| *Vim* | Integrated DNA Technologies | See Table S1 |
| **Recombinant DNA** | | |
| XBP1 reporter | Principal Investigator: Sanjeev Gupta<br>Samali et al.[50] | |
| **Software and algorithms** | | |
| Schrodinger Small Molecule Drug Discovery suite | https://www.schrodinger.com/ | RRID:SCR_014879 |
| UCSF Chimera | http://plato.cgl.ucsf.edu/chimera/ | RRID:SCR_004097 |
| MOE | http://www.chemcomp.com/MOE-Molecular_Operating_Environment.htm | RRID:SCR_014882 |
| MO.Affinity Analysis v2.3 | https://nanotempertech.com/monolith-mo-control-software/ | |
| GraphPad Prism | https://www.graphpad.com/ | RRID:SCR_002798 |
| **Other** | | |
| Monolith NT.115 Pico machine | NanoTemper, Munich, Germany | MO-G006-NB |

## RESOURCE AVAILABILITY

### Lead contact

Further information and requests for resources should be directed to and will be fulfilled by the lead contact, Dr Eric Chevet (eric.chevet@inserm.fr).

### Materials availability

This study did not generate new unique reagents. Primers sequences used were provided in Table S1, and available upon request to the corresponding author.

### Data and code availability

- The mass spectrometry proteomics data have been deposited to the ProteomeXchange Consortium via the PRIDE partner repository and is publicly available. Accession numbers are listed in the key resources table, Deposited data section.
- No original code was generated in this study.
- Any additional information required to reanalyse the data reported in this paper is available from the lead contact upon request.

## EXPERIMENTAL MODEL AND SUBJECT DETAILS

Cell lines – U87MG (U87; ATCC) cells were authenticated as recommended by AACR (http://aacrjournals.org/content/cell-line-authentication-information) and regularly tested for the absence of mycoplasma using MycoAlert (Lonza, Basel, Switzerland) or MycoFluor (Invitrogen, Carlsbad, CA, USA). U87 were grown in DMEM (Invitrogen, Carlsbad, CA, USA) supplemented with 10% FBS. GB immortalized U251 and primary RADH85 and RADH87[49] cells were grown in DMEM supplemented with 10% FBS in a 5% $CO_2$ humidified atmosphere at 37°C. GB cell lines were modified for IRE1 activity by overexpressing dominant negative (DN) forms of IRE1 that lack the RNase domain (IRE1.NCK or IRE1 Q780stop) as previously described.[26,51]

### Animal model

The *in vivo* study was performed on NMRI-Foxn1nu/Foxn1nu, 8 weeks old male mice purchased from Janvier Laboratories, Laval, France. All animal procedures met the European Community Directive guidelines (Agreement B35-238-40 Biosit Rennes, France/No DIR 13480) and were approved by the local (University of Rennes) ethics committee and ensuring the breeding and the daily monitoring of the animals in the best conditions of wellbeing according to the law and the rule of 3R (Reduce-Refine-Replace).

## METHOD DETAILS

### Materials

IRE1 wild-type recombinant protein encoding the cytoplasmic domain (amino acids 465–977) with *N*-terminal poly-histidine-tag and GST tag was purchased from Sinobiological (Sino Biological Europe GmbH, Eschborn, Germany, #11905-H20B). The fluorescent probe used for the *in vitro* IRE1 RNase assay was from Eurogentec (Cy3-CAUGUCCGCAGCGCAUG-BHQ3). Tunicamycin was purchased from Calbiochem (Merck KGaA, Darmstadt, Germany). All the inhibitors were synthesized by and purchased from Enamine (Riga, Latvia), with the exception of Z4P-(*R*) and Z4P-(*S*) which were obtained by chiral HPLC separation after resynthesis of racemic Z4P in-house (see chemical synthesis below).

### Chemical syntheses

#### *General information*

Commercially available reagents and solvents were purchased from Enamine, Fluorochem, Sigma-Aldrich, Alfa Aesar, Acros and were used as received. All reactions under inert atmosphere were performed under an argon atmosphere. Petroleum ether (PE) refers to petroleum ether with 40–60°C. Thin-layer chromatography (TLC) was performed on TLC silica gel 60 F254 aluminum plates. Compounds were visualized by exposure to UV light or by dipping the plates into potassium permanganate or phosphomolybdic acid solution followed by heating. Manual flash column chromatography was carried out using silica gel (particle size 40−63 μm) with step gradient elution as indicated. Automated flash column chromatography was carried out on an Interchim PuriFlash 450 using FlashPure Ecoflex silica cartridges (irregular particle size 50 μm) with NMR spectra were acquired on 300 MHz spectrometers and were referenced to the residual solvent.

All chemical shifts are reported in parts per million (ppm). Abbreviations used in the description of resonances are s (singlet), d (doublet), t (triplet), q (quartet), sept (septet), a (apparent), bs (broad singlet), and m (multiplet). Coupling constants (J) are quoted to the nearest 0.1Hz. HPLC-MS analyses were performed on a Shimadzu Prominence system couple to an Advion ESI mass spectrometer using a Thermoscientific Hypersil Gold aQ column chromatography (5µm, 250 × 4.6 mm) [method: binary gradient, solvent A = H2O + 0.1% TFA, solvent B = MeCN + 0.1% TFA, flow = 1 mL/min, 20 to 100% A/B].

## Racemic Z4P synthesis

### *4-(4-methoxyphenyl)butan-2-amine*

To a 250 mL RB flask filled with methanol (150 mL) was added 4-(4-methoxyphenyl)butan-2-one (5 g, 28.05 mmol, 1 eq.) and ammonium acetate (12.97 g, 168.3 mmol, 6 eq.) and the reaction mixture was left to stir at room temperature for 30 min. Temperature is then lowered to 0°C with an ice bath and sodium cyanoborohydride (2.64 g, 42.07 mmol, 1.5 eq.) was added portion wise. The ice batch was then removed and the reaction left to stir overnight at room temperature. TLC monitoring indicated full consumption of the starting material and the reaction was subsequently quenched at 0°C by addition of HCl 1M (200 mL). After 15 min of stirring, the reaction mixture was concentrated by rotary evaporation to remove most of the methanol and then extracted with diethyl ether (2x100 mL). The aqueous layer is isolated and basified by addition of concentrated NaOH until pH ≥ 10, and then sodium chloride is added until saturation, followed by extraction with DCM (3x100 mL). The combined organic layers were dried over anh. $MgSO_4$, filtered, evaporated to dryness by rotary-evaporation and the residue dried under high-vacuum to yield 4.2 g of crude (83% yield, 80 to 85% yield on average). Crude product was pure enough to be used without further purification, but if needed, purification can be performed by silica gel column chromatography with gradient elution (100:0-90:10 DCM/MeOH).

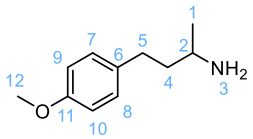


$^1$H NMR (300.16 MHz, $CDCl_3$, 20°C): δ = 7.10 (dt, 2H, C*H* 7,8); 6.82 (dt, 2H, C*H* 9,10); 3.78 (s, 3H, $CH_3$ 12); 2.90 (h, 1H, C*H* 2); 2.60 (qdd, 2H, $CH_2$ 5); 1.62 (m, 2H, $CH_2$ 4); 1.10 (d, 3H, $CH_3$ 1).

### *4-nitrophenyl (2,5-dimethylphenyl)carbamate*

To a 250 mL RB flask filled with dry AcOEt (100 mL) and under argon atmosphere was added successively the 4-nitrophenyl chloroformate (2.0 g, 9.9 mmol, 1.1 eq.) potassium carbonate (1.37 g, 9.9 mmol, 1.1 eq.) and 2,5-dimethylaniline (1.12 mL, 9.0 mmol, 1 eq.). The reaction is left stirring at room temperature and followed by TLC. After 2h, the reaction mixture is diluted with AcOEt (100 mL), transferred in a separatory funnel and washed successively with 1M citric acid (100 mL), sat. sodium carbonate (100 mL), and brine (100 mL). The organic layer is dried over anh. $MgSO_4$, filtered, evaporated to dryness by rotary-evaporation and the residue dried under high-vacuum to afford 1.9 g of (2,5-dimethylphenyl)carbamate (74% yield) as a pale beige solid, used without further purification.

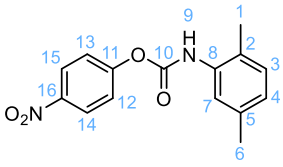


$^1$H NMR (300.16 MHz, $CDCl_3$, 20°C): δ = 8.29 (dt, 2H, C*H* 14,15); 7.64 (bs, 1H, N*H* 9); 7.41 (dt, 2H, C*H* 12,13); 7.11 (d, 1H, C*H* 3); 6.93 (d, 1H, C*H* 4); 6.78 (bs, 1H, C*H* 7); 2.32 (d, 6H, $CH_3$ 1,6).

### *1-(2,5-dimethylphenyl)-3-(4-(4-methoxyphenyl)butan-2-yl)urea*

To a 25 mL RB flask filled with dry DCM (12 mL) and under argon atmosphere was added 4-nitrophenyl (2,5-dimethylphenyl)carbamate (639 mg, 2.231 mmol, 1 eq.) and triethylamine (311 µL, 2.231 mmol, 1 eq.), followed by the 4-(4-methoxyphenyl)butan-2-amine (400 mg, 2.231 mmol, 1 eq.). The reaction was left

stirring at room temperature and TLC monitoring showed full conversion after 1h. The reaction mixture was then concentrated to dryness by rotary-evaporation and the solid residue triturated and sonicated in diisopropyl ether (10 mL), then filtered. The solid was collected and resuspended in cold water (10 mL) to be sonicated, followed by filtration (repeat twice). Finally, the solid was collected and dried under high-vacuum to afford 564 mg of 1-(2,5-dimethylphenyl)-3-(4-(4-methoxyphenyl)butan-2-yl)urea (77% yield) as a pale white solid, used without further purification.

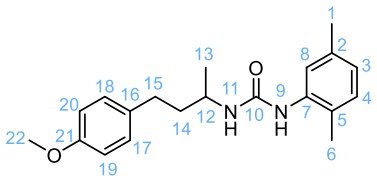

$^{1}$H NMR (300.16 MHz, $(CD_3)_2SO$, 20°C): δ = 7.81 (s, 1H, N*H* 9); 7.67 (s, 1H, C*H* 8); 7.12 (dt, 2H, C*H* 17,18); 6.95 (d, 2H, C*H* 3,4); 6.83 (dt, 2H, C*H* 19, 20); 6.64 (d, 1H, N*H* 11); 3.70 (s, 3H, C$H_3$ 22); 3.55 (m, 1H, C*H* 12); 2.56 (m, 2H, CH2 15); 2.20 (s, 3H, C$H_3$ 1); 2.14 (s, 3H, C$H_3$ 6); 1.64 (sept, 2H, C$H_2$ 14); 1.08 (d, 3H, C$H_3$ 13).

*1-(2,5-dimethylphenyl)-3-(4-(4-hydroxyphenyl)butan-2-yl)urea (Z4P)*

To a 100 mL RB flask filled with dry DCM (30 mL), under argon atmosphere was added 1-(2,5-dimethylphenyl)-3-(4-(4-methoxyphenyl)butan-2-yl)urea (300 mg, 0.92 mmol, 1 equiv eq.). After cooling to 0°C, boron tribromide (1M in DCM, 4.6 mL, 5 eq.) was added slowly over the course of a few minutes. The reaction mixture was left stirring for 1h at 0°C, and then warmed to room temperature and left stirring overnight. TLC monitoring showed full consumption of the starting material and the reaction was quenched by addition of ice (20 g) and stirred for 30 minutes before being transferred to a separatory funnel. Layers were separated and the aqueous layer extracted with DCM (2 x 40 mL) and AcOEt (2 x 40 mL). The combined organic layers were dried over anh. $MgSO_4$, filtered, evaporated to dryness by rotary-evaporation and the residue dried under high-vacuum to yield 258 mg of crude. 50 mg of crude product was purified by silica gel column chromatography (3g Silica, ratio 1:60) with solid loading and isocratic elution (75:25 EP/Acetone) to afford 47 mg of 1-(2,5-dimethylphenyl)-3-(4-(4-hydroxyphenyl)butan-2-yl)urea (Z4P) as a white powder.

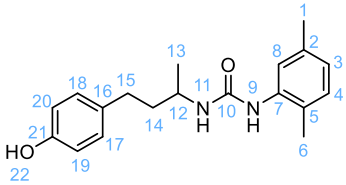

$^{1}$H NMR (300.16 MHz, $(CD_3)_2CO$, 20°C): δ = 8.10 (bs, 1H, O*H* 22); 7.80 (s, 1H, N*H* 9); 7.09 (s, 1H, C*H* 8); 7.03 (dt, 2H, C*H* 17,18); 6.97 (d, 1H, C*H* 4); 6.74 (dt, 2H, C*H* 19,20); 6.69 (d, 1H, C*H* 3); 5.92 (d, 1H, N*H* 11); 3.87 (sept, 1H, C*H* 12); 2.60 (m, 2H, CH2 15); 2.24 (s, 3H, C$H_3$ 1); 2.15 (s, 3H, C$H_3$ 6); 1.71 (m, 2H, C$H_2$ 14); 1.16 (d, 3H, C$H_3$ 13). $^{13}$C NMR (75.47 MHz, $(CD_3)_2CO$, 20°C): δ = 156.3 (*C* 21); 155.9 (*CO* 10); 139.2 (*C* 16); 136.3 (*C* 2); 133.8 (*C* 7); 130.7 (CH 4); 130.1 (CH 17,18); 124.8 (*C* 5); 123.7 (CH 3); 122.5 (C 7); 115.92 (CH 19,20); 46.0 (CH 12); 40.4 (C$H_2$ 14); 32.3 (C$H_2$ 15); 21.8 (C$H_3$ 13); 21.3 (C$H_3$ 1); 17.7 (C$H_3$ 6). MS (ESI+): *m/z* (%) 313.2 (100) [M+H$^+$]. *Chiral HPLC separation* - The preparative chiral HPLC separation was performed on an Agilent 1260 Infinity unit (pump G1311C, autosampler G1329B, DAD G1365D and fraction collector G1364C), and monitored by Agilent OpenLAB CDS Chemstation LC. Samples were dissolved in a mixture of ethanol and hexane (50/50) and eluted on a Chiralpak ID (250 × 10 mm) column, with hexane / ethanol / dichloromethane (80/10/10) as mobile phase, flow-rate = 5 mL/min, UV detection at 254 nm, yielding two enantiomers ($RT_A$ = 7.28 min and $RT_B$ = 9.12 min) with ee> 99.5%. *Optical rotary power measurements* - Absolute stereochemistry of enantiomers A and B were determined by measuring their optical rotary power and compared with a Z4P enantiomer of known stereochemistry, Z4P-*R* (in-house synthesis). Measurements were performed on

Perkin Elmer polarimeter 341 with sodium lamp (589 nm) and 1-dm path at 20°C using 0.5 mg/mL solutions of enantiomer A, enantiomer B and Z4P-*R* in acetonitrile. Results are the average of 3 measurements (1s integration time). Enantiomer A: average optical rotation −0.023°, $[\alpha]_D$ = - 46; Enantiomer B: average optical rotation +0.021°, $[\alpha]_D$ = +42; Z4P-*R*: average optical rotation +0.023°, $[\alpha]_D$ = + 46. Enantiomer A = Z4P-*S* & Enantiomer B = Z4P-*R*.

### *In silico* drug analyses

#### *Docking*

IRE1 protein structure (PDB IDs 3P23 & 4U6R) and libraries of compounds were prepared using Maestro Suites 2015–2018 (Schrödinger Release 2018-4: Schrödinger, LLC, New York, NY, 2018) and specifically utilizing tools within this program such as LigPrep, Glide Dock, Pharmacophore Hypothesis Generation, Glide grid generation and Protein preparation. Structural exploration and peptides preparation were carried out using software Supermimic[52] and MOE (MOE 2018.01: Chemical computing group, Montreal Canada), respectively. UCSF Chimera[53] was used for image generation developed by the Resource for Biocomputing, Visualization, and Informatics at the University of California, San Francisco, with support from NIH P41-GM103311. Hypotheses were tested against ZINC15 and FDA databases using the Supercomputer cluster Hebbe at the C3SE supercomputing centre (Sweden). Potential ADME properties were investigated using QikProp from Maestro Suites 2015–2018 (Schrödinger Release 2018-4: QikProp, Schrödinger, LLC, New York, NY, 2018) as well as swissADME.[37] *Boiled egg model* –Ligand Central Nervous System parameters and boiled-egg diagrams were calculated using SwissADME,[37,54] a comprehensive and free-to-use web portal developed and maintained by the Molecular Modeling Group of the Swiss Institute of Bioinformatics (SIB).

### MicroScale Thermophoresis (MST)

The direct binding of the Z4 and Z4P compounds to IRE1 protein was measured using MST. IRE1 recombinant protein was labelled using RED-Tris-NTA fluorescent dye (RED-Tris-NTA 2$^{nd}$ Generation, NanoTemper, Munich, Germany; # MO-L018). For the labelling step, 100 μL of 20 nM protein solution is mixed with 100 μL of 10 nM RED-Tris-NTA dye in PBST buffer (PBS with 0.05% Tween-20) and incubated for 30 min at RT. The protein–dye mixture was centrifuged for 10 min at 4°C and 15 000*xg*. For measurement of direct binding, the compounds were analyzed in a 16-point dilution series mixed in a 1:1 ratio with the labelled protein in PBST buffer. The assay was performed in standard Monolith NT.115 Capillaries (NanoTemper; #MO-K022), and all measurements were performed at 60% MST power and 60% excitation power using the Monolith NT.115 Pico machine (NanoTemper). The dissociation constant (Kd) was calculated by taking the average of triplicate normalized fluorescence data using NANOTEMPER analysis software (MO.Affinity Analysis v2.3). The normalized values were converted to fraction-bound data, and the resulting binding curves are plotted using GRAPHPAD PRISM software (GraphPad Software).

### IRE1-mediated *in vitro* RNase assay

Stock solution of organic molecules were diluted in minimal volume of DMSO and subsequently re-diluted in reaction buffer (20 mM HEPES pH 7.5; 1 mM MgOAc; 50 mM KOAc). Maximum volume of DMSO per reaction never exceeded 1%. Reaction volume was 25 μL. Recombinant IRE1 (0.6 μg/reaction) was incubated at room temperature for 10 minutes with varying concentrations (0–100 μM) of inhibitor and reaction buffer. The assay relied on the use of fluorescence-quenched mini XBP1 RNA substrate probe, which when cleaved by IRE1 emits fluorescence at 590 nm (cy5) wavelength.[55] Subsequently equal volume of mixture of reaction buffer, 20 mM ATP, 2 mM DTT and 1 μg of fluorescent probe were added to each sample and fluorescence was read in 96 well plates flat bottom, black polystyrene, matrix active group High Bind (Corning®) every minute for 25 minutes, at 37°C, using a Tecan 200 plate reader.

### Cell treatments

For XBP1s induction experiments, tunicamycin was used at 1 μg/mL for the indicated periods of time. For inhibitor cell toxicity assays, cells were plated in 96 well plates at 5000 cells per well and treated with 0, 5, 10, 25, 50, 100, 250, 500, 1000 and 2500 μM concentrations of each inhibitor. After 6 days of incubation, WST1 reagent (Roche) was added to each well and post 2-hour incubation the plate was read using a Tecan 200 colorimeter. For TMZ sensitivity assays, cells were plated in a 96 well plate at 5000 cells per well and co-treated with 0, 5, 10, 25, 50, 100, 250, 500, 1000 and 2500 μM of TMZ plus a non-toxic dose of inhibitor. After

6 days of incubation, WST1 reagent (Roche) was added to each well and post 2-hour incubation the plate was read using a Tecan 200 colorimeter.

### Quantitative real-time PCR

Total RNA was prepared using TRIzol reagent (Invitrogen, Carlsbad, CA, USA). All RNAs were reverse-transcribed with Maxima Reverse Transcriptase (Thermo Scientific, Waltham, MA, USA), according to manufacturer protocol. qPCR was performed via a StepOnePlus™ Real-Time PCR Systems from Applied Biosystems and the SYBR Green PCR Core reagents kit (Takara). Analysis were carried out using QuantStudio™ Design and Analysis software version 1.3.1. Three technical repeats were performed per experiment and at least three biological repeats were performed per point per experiment. Each sample was extracted individually for RNA and the quantification of mRNA levels by qPCR for several targets was performed. These data were then plotted using Morpheus' tool from the Broad institute (https://software.broadinstitute.org/morpheus). The primers used in the qPCR analyses are presented in Table S1.

### Luciferase assays

Cells were seeded in 96-well plate and treated with increasing concentration of Z4 and analogues. Medium was discarded and the plate was tapped to remove residual medium. 100 µL of lysis buffer (25 mM Tricine pH 7.8; 15 mM Potassium Phosphate pH 7.8; 15 mM $MgSO_4$; 4 mM EGTA; 1% Triton X-100; 1 mM DTT) were added per well and incubated for 20 minutes at RT. 50 µL were transferred to a white 96-well plate and 50 µL of substrate buffer (25 mM Tricine pH 7.8; 15 mM Potassium Phosphate pH 7.8; 15 mM $MgSO_4$; 4 mM EGTA; 1% Triton X-100; 1 mM DTT; 1 mM ATP; 0.2 mM luciferin) were added in each well and the luminescence was read.

BBB permeability – Experiments were contracted to IRBM S.p.A and performed as described in Di Marco et al. (2021), Establishment of an *in Vitro* Human Blood-Brain Barrier Model Derived from Induced Pluripotent Stem Cells and Comparison to a Porcine Cell-Based System, Cells, *9(4)*, 994. 10.3390/cells9040994.[39]

Proteomic analyses – Untreated, MKC8866 and Z4-treated (during 48 hours) parental as well as DN IRE1 RADH87 GB cells were lysed with lysis buffer (20 mM Tris-HCl pH 8, 1.5 mM EDTA, 150 mM NaCl, 1% Triton X-100, 0.1% SDS) and phosphatases inhibitor cocktails (Roche). Total proteins were precipitated with 80% ice-cold acetone. Washed pellets were then denatured with 8 M urea in Tris-HCl 0.1 mM, reduced with 5 mM TCEP for 30 minutes, and then alkylated with 10 mM iodoacetamide for 30 minutes in the dark. Double digestion was performed using endoproteinase Lys-C (Ref 125–05061, Wako) at a ratio 1/100 (enzyme/proteins) in 8 M urea for 4h, followed by an overnight modified trypsin digestion (Ref V511A, Promega) at a ratio 1/100 (enzyme/proteins) in 2 M urea. Both Lys-C and Trypsin digestions were performed at 37°C. Peptide mixtures were then desalted on C18 spin-column and dried on Speed-Vacuum before LC-MS/MS analysis. Samples were analyzed using an Ultimate 3000 nano-RSLC (Thermo Fisher Scientific, San Jose California) coupled in line with a LTQ-Orbitrap ELITE mass spectrometer via a nano-electrospray ionization source (Thermo Scientific, San Jose California). Proteins were identified and quantified by database searching using SequestHT (Thermo Fisher Scientific) with Proteome Discoverer 2.4 software (PD2.4, Thermo Fisher Scientific) against *Homo sapiens* reviewed SwissProt database. Peptides and proteins were filtered with a false discovery rate (FDR) at 1% and their quantification was based on XIC (Extracted Ion Chromatogram). Raw data, Proteome Discoverer parameters and results are provided at PRIDE protein identification database. *Data Availability* - The mass spectrometry proteomics data have been deposited to the ProteomeXchange Consortium via the PRIDE partner repository with the dataset identifier PXD026908. The dataset is available at: http://www.ebi.ac.uk/pride.

Proteomic Data analyses and representation - Differential proteome expression analysis was executed to compare the impact of Z4 treatment and IRE1 genetic inhibition. The parental RADH87 cell lines were treated with Z4 or dimethyl sulfoxide (DMSO) and the resulting proteomes compared to that of the same lines expressing DN forms of IRE1 (IRE1.NCK or IRE1 Q780stop). Statistical analyses were based on the non-parametric method of rank products, using the RankProd (R/Bioconductor) package.[35] RP and topGene functions were utilized to identify the most significantly over- and under-expressed proteins, setting the p value threshold at 0.05. Differentially expressed proteins in the wild type – Z4-treatement comparison with absolute log fold change value lower than that of wild type - DMSO comparison, were filtered out, as their regulation cannot be exclusively attributed to the effect of Z4 administration. BioInfoMiner[56,57] was used for the functional interpretation of the sets of significantly perturbed proteins

and the comparative analysis of the derived semantic networks. Pathway analysis was performed, exploiting the annotation of Gene Ontology (Biological Process domain – GO-BP),[58] with hyper-geometric and adjusted p value thresholds at 0.05. A network of statistically important GO-BP terms was identified for each list of proteins. Then, all significantly over-represented terms were clustered, using the Resnik semantic similarity measure.[59] In each iteration of the agglomerative clustering process, the most similar pair of terms was substituted with its most informative common ancestor (mica). Semantic similarity threshold was set to 0.25, as lower values might produce semantic clusters, with overly generic semantic description. Examining the membership of each GO-BP cluster and the initial lists of over-represented terms, a binary association matrix was constructed, to reveal and compare the membership profiles of the regulated sets of proteins in cellular functionality.

### Western blotting

Cells grown on 6 well plates were washed with PBS and lysed with RIPA lysis buffer at 4°C, over 25 min to extract proteins. IRE1 and phosphorylated IRE1 were stained using anti-IRE1 antibody (Anti-human; rabbit polyclonal; SantaCruz Biotechnologies, H-190) and pS724-IRE1 antibody (Anti-human; rabbit polyclonal; Abcam, ab48187), respectively. The phosphorylated form of eIF2α was stained with anti-phospho-eIF2α (Ser51) Antibody #9721 (CellSignalling). Actin and VCP were used as a loading control (β-Actin (C4): sc-47778; SantaCruz Biotechnologies and VCP anti-mouse 612183 BD Transduction Lab). ATF4 was stained using ATF-4 (D4B8) Rabbit mAb #11815. Cell extracts were resolved by SDS-PAGE and transferred to nitrocellulose membranes for 30 min using a Trans-Blot Turbo (BioRad® Transfer System #1704150). The resulting membranes were incubated with primary antibodies for 16 hours at 4°C, washed with PBST, and incubated for 1 hour with goat anti-rabbit or goat anti-mouse secondary antibodies at room temperature (Invitrogen, Carlsbad, CA, USA) prior revelation using chemiluminescence (ECL RevelBlOt® Intense, Ozyme). Detailed protocols can be found in Lhomond et al., 2015.[60]

### Migration assay

Cells were seeded in 6-wells plates at the concentration of $10^5$ cells/mL and incubated overnight at 37°C, 5% $CO_2$. After incubation, the cells were treated with 25 μM of DMSO, and Z4 or its analogues (at the indicated concentrations) for 24 hours. Cells were trypsinized, then trypsin was quenched using 10% FBS and spun down. Cells were washed with serum-free medium, spun down again and resuspended at 1.5 x $10^5$ cells/mL in serum-free medium. Next, we used 24-well transwell plates (Transwell® Permeable Supports 6.5 mm inserts Costar® ref.3422). The bottom wells contained 400 μL of DMEM + 10% FBS. In each top chamber, we added 300 μL of serum-free medium and 100 μL of cells suspension. The plates were incubated for 24 hours at 37°C, 5% $CO_2$. After incubation, media was removed from the wells and the membranes stained with crystal violet for 30 minutes at RT. Visualization was performed using light microscopy and quantitation of images was carried out using ImageJ.

### Kinome selectivity profiling

Profiling was performed using Eurofins kinase profiler™ radiometric assay platform, which assess both selectivity and kinase activities. The Discovery Panel that includes 58 human kinases representative of all major kinome branches was selected to evaluate the hit compounds selectivity at a fixed concentration of 10 μM. Details about Kinase Profiler™ and the Discovery Panel are available at https://www.eurofinsdiscoveryservices.com/services/in-vitro-assays/kinases/kinase-profiler.

### Tumor cell orthotopic implantation

Tumor cells (U87-Luc[48]) were implanted into the brain of immunodeficient NMRI-Foxn1nu/Foxn1nu, 8 weeks old male mice (Janvier Laboratories, Laval, France). U87-Luc cells were implanted in the mouse brain by intracerebral injection followed by tumor growth monitoring using bioluminescence (PhotonIMAGER™ systems, BIOSPACE LAB). Mice were anesthetized using intra-peritoneal (i.p.) injection of Xylazine 10 mg/kg and Ketamin 60 mg/kg and then fixed on a stereotactic frame. This framework makes it possible to manipulate the brains of living animals, and to reach isolated areas of the brain precisely relative to markings visible to the naked eye through the use of three-dimensional coordinates. After incising the scalp, the stereotaxic coordinates were calculated for injection of tumor cells into a specific point of the brain, and reproducible for all the mice used. In the study, the tumor cells (5 x $10^4$ cells per mice in 1 μL) were injected at Bregma 0, 2.2 mm to the left of the bregma and 3.2 mm deep to perform the implantation at the level of the striatum.

### Mouse treatments

Four days after tumor cells implantation, Z4P treatments were started consisting in treatments of 300 μg/kg/day intraperitonially. For the RNA quantification experiment, performed on tumors generated in mice, three mice per group were treated according to the methods above. Mice were sacrificed at day 34 and the brains were removed and the tumors extracted. The samples were used to extract RNA for the analysis, as described below. For the survival experiment, performed on tumors generated in mice, co-treatment with TMZ was performed one week after the beginning of Z4 treatment (n = 7 per group for the TMZ and COMBO, n = 8 per group for the control and Z4P). The animals were injected with 10 mg/kg/day of TMZ delivered intraperitoneally for ten days. All the treatments were performed with 2 days of rest each week. Survival was measured as the time between implantation and sacrifice, which was performed by cervical dislocation in case of critical clinical signs or loss of weight >10%.

### Bioluminescence monitoring

Mice were evaluated with *in vivo* bioluminescence imaging every 3 days starting from the day 4, for the first week, and weekly onward for tumor progression and followed for signs of neurologic deterioration daily. Mice were injected intra-peritoneally with 100 μL of luciferin (Promega, Charbonnières-les-Bains, France). Luciferin was allowed to circulate for 5 min before the mice were anesthetized with a mix of $O_2$ and isoflurane (2.5%).

### Immunohistochemistry

The immunochemistry experiments were performed on 5 μm tumor sections which were incubated at room temperature for 1 hour with primary antibodies. Immunostaining was performed using BenchMarkXT-Ventana Medical Systems with kit OMNIMAP (system "biotin-free" using multimer technology) with antigen retrieval for all (Tris/borate/EDTA pH 8). To perform the analysis, glass slides were converted on to digital slides with the scanner Nanozoomer 2.0-RS Hamamatsu.

### Quantification and statistical analysis

Data are presented as mean ± SEM or ± SD as indicated in each figure. Statistical significance ($p < 0.05$) was determined using unpaired *t*-tests or ANOVA as appropriate and performed using GraphPad Prism software (GraphPad Software, San Diego, CA, USA). Curve's extrapolations were performed using curve fit hypotheses by GraphPad Prism software (GraphPad Software, San Diego, CA, USA).